Flux reconstruction method for time-harmonic linear propagation problems: 1D a priori error analysis

Matthias Rivet, Sébastien Pernet, Sébastien Tordeux

Mathematical Modelling and Numerical Analysis Will be set by the publisher
Modélisation Mathématique et Analyse Numérique

FLUX RECONSTRUCTION METHOD FOR TIME-HARMONIC LINEAR PROPAGATION PROBLEMS: 1D A PRIORI ERROR ANALYSIS

Matthias Rivet[1], Sébastien Pernet[2] and Sébastien Tordeux[3]

Abstract. The Flux Reconstruction (FR) method is well established for hyperbolic equations in the Computational Fluid Dynamics field, but has barely been studied for electromagnetism. In this article, we propose to describe the FR formulation for time-harmonic linear hyperbolic problems. In particular, this formalism includes the Maxwell's equations and the unidimensional wave equations, for which the method is detailed. We then focus on the wave equations for incoming boundary conditions, and prove the well-posedness of the associated FR method and quasi-optimal a priori error estimates, which are explicit in terms of the flux correction polynomials and discretisation parameters. Numerical experiments finally validate the main behaviours of the estimates, and confirm the good properties of the method for the Maxwell problem.

Résumé. La méthode *Flux Reconstruction* (FR) est largement établie pour les équations hyperboliques de la mécanique des fluides, mais n'a été encore que peu étudiée dans le cadre de l'électromagnétisme. Dans cet article, nous nous proposons donc de décrire la formulation FR pour des problèmes hyperboliques linéaires harmoniques. Ce formalisme général contient en particulier le problème de Maxwell et l'équation des ondes unidimensionnelle, pour lesquelles la méthode est détaillée. Nous nous concentrons ensuite sur l'équation des ondes pour des conditions de bord entrantes, et prouvons le caractère bien posé de la méthode FR associée, ainsi que des estimations d'erreur a priori quasi-optimales et explicites en les polynômes de correction de flux et les paramètres de discrétisation. Finalement, des expériences numériques permettent de valider les principaux comportements de ces estimations, et confirment les bonnes propriétés de la méthode pour les équations de Maxwell.

2020 Mathematics Subject Classification. 65N12, 65N35, 35L02, 35Q61.

22/12/2023.

Introduction

Electromagnetic waves propagation is a fundamental physical phenomenon at the heart of many science and engineering fields: their numerical simulation therefore represents a considerable stake and has led to the development and adaptation of numerous methods. In particular, the Finite Difference Method (FDM) [8, 40, 46]

Keywords and phrases: Hyperbolic problem, Time-harmonic equations, Flux Reconstruction method, High-order approximation, Maxwell's equations, A priori error estimate

[1] ONERA/DTIS, Université de Toulouse F-31055 Toulouse - France & EPI Makutu, Inria, Université de Pau et des Pays de l'Adour, TotalEnergies, CNRS UMR 5142

[2] ONERA/DTIS, Université de Toulouse F-31055 Toulouse - France

[3] EPI Makutu, Inria, Université de Pau et des Pays de l'Adour, TotalEnergies, CNRS UMR 5142

is the first approach which has been introduced to deal with Maxwell's equations. Then, the search of high-order methods gave rise to the Finite Element Method (FEM) [1, 3, 7, 8, 16, 23, 30], the Discontinuous Galerkin (DG) [7, 17, 18, 35] or the Boundary Element Method (BEM) [4, 38] for example: these classic approaches are thus widely used in both academic and industrial contexts. This inexhaustive list of methods and articles embodies the broad spectrum of strategies which have been considered to face time-harmonic problems, with two main point of views: weak-formulations for DG and FEM in opposition to strong ones for FDM.

At the same time, the Computational Fluid Dynamics (CFD) community particularly focused on Finite Volume Method (FVM), which are commonly used in industrial configurations at relatively low order. The recent increase in computational abilities has also elicited interest for high-order methods. This tends to accelerate the spreading of the Flux Reconstruction (FR) method, which is the topic of this article, and of the DG ones, which have intensively been studied for wave propagation problems. The FR method was first introduced by Huynh [20] and relies on the strong formulation with a hyperbolic point of view: the solution and flux approximations are searched as piecewise polynomial functions of degree k and $k+1$ respectively. To take Boundary Conditions (BCs) and continuity properties into account, the flux variables result from the use of correction polynomial functions.
Such high-order methods relying on the strong formulation had particularly gained interest with the introduction of the staggered-grid method [24], which was then extended to triangular cells by Liu et al. [26] and renamed Spectral Difference (SD). Such a generalisation for FR has been introduced in [44] through a method named Lifting Collocation Penalty: both methods were lately gathered under the denomination of Correction Procedure via Reconstruction (CPR). As this article will only consider the classic framework of FR, we will stick to this designation in what follows. Further developments were then led for Euler and Navier-Stokes equations in 2 and 3 dimensions on various mesh types. More generally, a class of energy-stable schemes, referred as Energy Stable Flux Reconstruction (ESFR) or Vincent-Castonguay-Jameson-Huynh (VCJH), tends to bring a pertinent approach to the construction of high-order stable methods for these time-dependent problems [22, 43]. Finally, entropy stability considerations start to be taken into account in recent studies [27]. The reader may consult the reviews [21, 45] for an overview of the main developments of the method up to 2015.
In terms of noteworthy properties, the FR method relies on a strong formulation which does not depend on any quadrature rule and offers a generic way to create high-order accurate methods (by choosing different definitions for the flux correction polynomial functions). Moreover, classic methods can be retrieved with this construction scheme in usually less sophisticated and expensive ways, such as particular SD and nodal DG methods [20, 44]: their good sparsity and conditioning properties can then be obtained in this framework. In particular, the close relationships between a class of FR and filtered DG have been investigated by Allaneau and Jameson [2], offering an alternative view of the stability criterion of Vincent et al [43]. Last but not least, this formalism allows an easy understanding of the method effects (by being able to compute the flux correction polynomial functions and their properties) while intrinsically respecting the hyperbolic structure of the equation.

The objective is then to adapt the FR approach to time-harmonic wave propagation problems. Indeed, due to the non-linear properties of CFD equations, most of the FR developments have been realised in a time-dependent context for transport, Euler and Navier-Stokes equations: to our knowledge, only a few adaptations to the transient Maxwell equations have already been realised for transverse electric and magnetic waves [14, 26], and in the specific case of SD [37]. We will then detail the method in a general framework of time-harmonic linear hyperbolic problems, which includes acoustic, elastic and electromagnetic wave equations. In particular, this paper deals with both Maxwell's equations and the 1D wave equations, for a Cartesian mesh. The question of the well-posedness of the associated FR methods then naturally arises, which leads us to derive such conditions for a specific case of the 1D wave equations, by leaning on the uncoupling property of one-way variables. Moreover, while most of the theoretical study of the FR methods relies on Fourier (Von Neumann) analysis, we derive a priori error estimates in Sobolev norms in this framework to explicit the impact of flux correction polynomial functions on the method.

This paper is organised as follows. We first introduce our two problems of interest, the time-harmonic 1D wave equations and 3D Maxwell problem, in addition to a more general time-harmonic linear hyperbolic setting. Section 2 describes the associated FR method and details the flux reconstruction procedure, in particular for numerical traces obtained through a generic metric-based flux operator decomposition. Then, Section 3 specifies the FR method we consider for both model problems. This introduction allows to derive a priori explicit error estimates for the 1D wave equations with ingoing boundary conditions in Section 4. Finally, such estimates are numerically illustrated in Section 5 and the FR implementation for Maxwell's equations is validated in Section 6 thanks to classic exact solutions.

1. The FR method for a time-harmonic linear hyperbolic problem

This article focuses on two specific time-harmonic equations: the homogeneous 1D wave equations and the 3D Maxwell problem, that we will briefly recall. We also introduce a general linear hyperbolic framework (including these two cases) which will allow us to develop a generic description of the associated FR method.

1.1. Introduction of the problems of interest

First, we introduce the two problems on which we will focus and detail the FR approach.

1.1.1. *The homogeneous time-harmonic 1D wave equations*

The first model problem we consider in this article is the 1D time-harmonic wave problem written in its hyperbolic form. Its interest is purely theoretical and does not lie in its discretisation.

Problem 1.1 (Time-harmonic 1D wave problem)**.** Let $\Omega := [0, L] \subset \mathbb{R}$ be an interval and $\kappa > 0$ be the wavenumber. Find $\mathbf{y} = (u, v)^T \in \left[\mathrm{H}^1(\Omega)\right]^2$ such that

$$i\kappa\mathbf{y} + \frac{\mathrm{d}\boldsymbol{\phi}}{\mathrm{d}x} = \mathbf{0} \quad \text{with} \quad \boldsymbol{\phi} = \mathbf{F}(\mathbf{y}) \quad \text{in } \Omega, \tag{1}$$

equipped with Fourier-Robin Boundary Conditions (BCs) written as

$$u(0) - Z_1 v(0) = g_1 \quad \text{and} \quad u(L) + Z_2 v(L) = g_2, \tag{2}$$

with the linear flux operator $\mathbf{F} = \begin{pmatrix} 0 & -1 \\ -1 & 0 \end{pmatrix}$, $Z_1, Z_2 \in \{Z \in \mathbb{C} \,:\, \Re(Z) > 0\}$, and $(g_1, g_2) \in \mathbb{C}^2$.

Remark 1.2. The simplest way to obtain this system is to consider the time-harmonic solution $\mathbf{Y} = (U, V)$, with $U(x,t) = \Re\left(u(x)e^{i\omega t}\right)$ and $V(x,t) = \Re\left(u(x)e^{i\omega t}\right)$, of the d'Alembert equation written in a hyperbolic way

$$\frac{\partial V}{\partial x}(x,t) \,-\, \frac{1}{c}\frac{\partial U}{\partial t}(x,t) \,=\, 0 \quad \text{and} \quad \frac{\partial U}{\partial x}(x,t) \,-\, \frac{1}{c}\frac{\partial V}{\partial t}(x,t) \,=\, 0 \quad \text{for } (x,t) \in \Omega \times \mathbb{R}, \tag{3}$$

equipped with the Fourier-Robin boundary conditions

$$U(0,t) - Z_1 V(0,t) = \Re\left(g_1 \exp(i\omega t)\right) \quad \text{and} \quad U(L,t) + Z_2 V(L,t) = \Re\left(g_2 \exp(i\omega t)\right), \tag{4}$$

with $\omega > 0$ the angular frequency and $c > 0$ the velocity, such that $\kappa = \dfrac{\omega}{c}$.

Remark 1.3. We recall that the 1D time-harmonic wave problem 1.1 is well-posed for $Z_1, Z_2 \in \{Z \in \mathbb{C} \,:\, \Re(Z) > 0\}$. It can be solved analytically by introducing $y^{\rightarrow} = u - v = \alpha e^{-i\kappa x}$ and $y^{\leftarrow} = u + v = \beta e^{i\kappa x}$ whose amplitudes α, β are solutions of

$$\left\{ \begin{array}{ccccccc} (1+Z_1) & \alpha & + & (1-Z_1) & \beta & = & 2g_1, \\ (1-Z_2)e^{-i\kappa L} & \alpha & + & (1+Z_2)e^{i\kappa L} & \beta & = & 2g_2, \end{array} \right. \tag{5}$$

with the determinant $\delta = 2\cos(\kappa L)(Z_1 + Z_2) + 2i\sin(\kappa L)(1 + Z_1 Z_2) \neq 0$.
This decomposition will find its usefulness in the estimates proof of Section 4.

1.1.2. *The time-harmonic 3D Maxwell problem*

Then, we introduce the time-harmonic 3D Maxwell problem, as a more complex problem (not being in one dimension anymore will call on a few subtleties): its importance for industrial problematics justifies the design of adapted FR methods.
Let's consider an orthogonal parallelepiped domain $\Omega \subset \mathbb{R}^3$, whose boundary is denoted as $\partial\Omega$. The vacuum permittivity and permeability are denoted as ϵ_0 and μ_0, while the relative ones are respectively ϵ_r and μ_r, and we suppose they verify the conditions outlined in Section 4.2 of [30]. Then, in the absence of charges and currents, the Maxwell problem for the electric and magnetic fields $\mathbf{E}$ and $\mathbf{H}$ takes the form

$$\forall\ (\mathbf{x}, t) \in \Omega \times \mathbb{R}^+,\ \begin{cases} \boldsymbol{\nabla} \times \mathbf{E}(\mathbf{x}, t) &= -\dfrac{\partial \mathbf{B}}{\partial t}(\mathbf{x}, t), \\ \boldsymbol{\nabla} \times \mathbf{H}(\mathbf{x}, t) &= \dfrac{\partial \mathbf{D}}{\partial t}(\mathbf{x}, t), \end{cases} \tag{6}$$

with, in the case of a linear and isotropic material,

$$\mathbf{D} = \epsilon_0 \epsilon_r \mathbf{E} \quad \text{and} \quad \mathbf{B} = \mu_0 \mu_r \mathbf{H}. \tag{7}$$

We obtain the time-harmonic version by looking for $\mathbf{E}$ and $\mathbf{H}$ as

$$\mathbf{E}(\mathbf{x}, t) = E_0\ \Re\left(\mathbf{e}(\mathbf{x})\ e^{i\omega t}\right) \quad \text{and} \quad \mathbf{H}(\mathbf{x}, t) = H_0\ \Re\left(\mathbf{h}(\mathbf{x})\ e^{i\omega t}\right), \tag{8}$$

denoting their amplitudes as E_0 and $H_0 = \sqrt{\dfrac{\epsilon_0}{\mu_0}}\ E_0$, the speed of light in a vacuum as $c_0 = (\epsilon_0\ \mu_0)^{-1/2}$ and the wavenumber as $\kappa = \dfrac{\omega}{c_0}$. This finally leads to the following normalised time-harmonic Maxwell equations that we equip with impedance BCs.

Problem 1.4 (Time-harmonic Maxwell problem)**.** Find the electromagnetic field $\mathbb{E} := (\mathbf{e}, \mathbf{h}) \in \left[\mathrm{L}^2(\Omega)\right]^6$ s.t.

$$\begin{cases} i\kappa \mathbf{M}\mathbb{E} + \dfrac{\partial \boldsymbol{\phi}^x}{\partial x} + \dfrac{\partial \boldsymbol{\phi}^y}{\partial y} + \dfrac{\partial \boldsymbol{\phi}^z}{\partial z} = \mathbf{0} & \text{in } \Omega, \\ \boldsymbol{\phi}^x = \mathbf{F}^x \mathbb{E}, \quad \boldsymbol{\phi}^y = \mathbf{F}^y \mathbb{E} \quad \text{and} \quad \boldsymbol{\phi}^z = \mathbf{F}^z \mathbb{E} & \text{in } \Omega, \\ \gamma_t[\mathbf{n}_{\partial\Omega}]\mathbf{e}\ +\ Z_{\partial\Omega}\ \gamma_\times[\mathbf{n}_{\partial\Omega}]\mathbf{h} = \mathbf{g} & \text{on } \partial\Omega, \end{cases} \tag{9}$$

by denoting

$$\begin{gathered} \mathbb{E}\ =\ (e_x\, e_y, e_z, h_x, h_y, h_z)^T, \quad \mathbf{M}\ =\ \begin{bmatrix} \varepsilon_r \mathbf{I}_3 & \mathbf{0}_3 \\ \mathbf{0}_3 & \mu_r \mathbf{I}_3 \end{bmatrix}, \\ \mathbf{F}^x = \begin{bmatrix} \mathbf{0}_3 & -\boldsymbol{\Gamma}_\times[\mathbf{e}_x] \\ \boldsymbol{\Gamma}_\times[\mathbf{e}_x] & \mathbf{0}_3 \end{bmatrix}, \quad \mathbf{F}^y = \begin{bmatrix} \mathbf{0}_3 & -\boldsymbol{\Gamma}_\times[\mathbf{e}_y] \\ \boldsymbol{\Gamma}_\times[\mathbf{e}_y] & \mathbf{0}_3 \end{bmatrix} \quad \text{and} \quad \mathbf{F}^z = \begin{bmatrix} \mathbf{0}_3 & -\boldsymbol{\Gamma}_\times[\mathbf{e}_z] \\ \boldsymbol{\Gamma}_\times[\mathbf{e}_z] & \mathbf{0}_3 \end{bmatrix}, \end{gathered} \tag{10}$$

where $Z_{\partial\Omega} \in \mathrm{L}^\infty(\partial\Omega)$ denotes the positive boundary impedance that we suppose constant on each face, $\mathbf{g} \in \left[\mathrm{L}^2(\partial\Omega)\right]^3$ and $\mathbf{I}_3$ and $\mathbf{0}_3$ stand for the identity and null matrices of $\mathbb{C}^{3,3}$.
The tangential component and trace of $\mathbf{w}$ are denoted on $\partial\Omega$ as

$$\gamma_t[\mathbf{n}_{\partial\Omega}]\mathbf{w} = \mathbf{w} - (\mathbf{w} \cdot \mathbf{n}_{\partial\Omega})\ \mathbf{n}_{\partial\Omega} = (\mathbf{n}_{\partial\Omega} \times \mathbf{w}) \times \mathbf{n}_{\partial\Omega} \quad \text{and} \quad \gamma_\times[\mathbf{n}_{\partial\Omega}]\mathbf{w} = \mathbf{n}_{\partial\Omega} \times \mathbf{w}, \tag{11}$$

where $\mathbf{n}_{\partial\Omega}$ stands for the outgoing normal from the domain Ω.
The matrices associated to these operators for a vector $\mathbf{n} = (n_1, n_2, n_3)$ are denoted as $\mathbf{\Gamma}_t[\mathbf{n}]$ and $\mathbf{\Gamma}_\times[\mathbf{n}]$ with

$$\mathbf{\Gamma}_\times[\mathbf{n}] = \begin{bmatrix} 0 & -n_3 & n_2 \\ n_3 & 0 & -n_1 \\ -n_2 & n_1 & 0 \end{bmatrix} \quad \text{and} \quad \mathbf{\Gamma}_t[\mathbf{n}] = -\left(\mathbf{\Gamma}_\times[\mathbf{n}]\right)^2 = \begin{bmatrix} (n_2)^2+(n_3)^2 & -n_1n_2 & -n_1n_3 \\ -n_1n_2 & (n_1)^2+(n_3)^2 & -n_2n_3 \\ -n_1n_3 & -n_2n_3 & (n_1)^2+(n_2)^2 \end{bmatrix}, \tag{12}$$

such that one has $\gamma_t[\mathbf{n}]\mathbf{w} = \mathbf{\Gamma}_t[\mathbf{n}]\mathbf{w}$ and $\gamma_\times[\mathbf{n}]\mathbf{w} = \mathbf{\Gamma}_\times[\mathbf{n}]\mathbf{w}$.

Theorem 1.5 (Monk)**.** *Problem* 1.4 *is well-posed for* $\mathbf{g} \in \mathrm{L}^2_t(\partial\Omega)$*, with*

$$\mathrm{L}^2_t(\partial\Omega) = \left\{ \mathbf{w} \in \left[\mathrm{L}^2(\partial\Omega)\right]^3 \ : \ \mathbf{w}\cdot\mathbf{n}_{\partial\Omega} = 0 \right\}. \tag{13}$$

Proof. By referring to Theorem 4.17 of [30], Ω, ϵ_r, μ_r and $Z_{\partial\Omega}$ all satisfy its conditions of application, which ensures the well-posedness of the problem. □

1.2. **The abstract hyperbolic setting**

After developing the two specific systems on which we will specify the FR method, we propose a framework for general linear hyperbolic problems.
Let $p, q \in \mathbb{N}^*$ and $\Omega \subset \mathbb{R}^p$ be a p-hyperrectangular domain, whose $2p$ faces are denoted as $(\partial\Omega_s)_{s\in[\![1,2p]\!]}$.

For a given Right Hand Side (RHS) $\boldsymbol{\psi} \in \left[\mathrm{L}^2(\Omega)\right]^q$ and $\kappa > 0$, we consider a time-harmonic hyperbolic system

$$i\kappa\mathbf{M}\mathbf{y} + \sum_{j=1}^{p} \frac{\partial \boldsymbol{\phi}^j}{\partial x_j} = \boldsymbol{\psi} \quad \text{in } \Omega, \tag{14}$$

governing the primal variable $\mathbf{y} : \Omega \to \mathbb{C}^q$ related to dual variables $\boldsymbol{\phi}^j : \Omega \to \mathbb{C}^q$, for $j \in [\![1,p]\!]$, by the flux operator $\mathbf{F}^j \in \mathbb{R}^{q,q}$ as

$$\boldsymbol{\phi}^j = \mathbf{F}^j\mathbf{y}. \tag{15}$$

In this paper, we suppose that $\mathbf{M} \in \mathbb{R}^{q,q}$ denotes a symmetric positive definite metric operator and that the $\mathbf{F}^j$ are all symmetric, which implies the classical hyperbolic hypothesis that $\mathbf{F}[\boldsymbol{\xi}] = \xi_1\mathbf{F}^1 + \cdots + \xi_p\mathbf{F}^p$ is diagonizable in $\mathbb{R}$ for any $\boldsymbol{\xi} \in \mathbb{R}^p$.
We assume this equation is equipped with boundary conditions

$$\mathbf{B}\mathbf{y} = \mathbf{B}\mathbf{y}_{BC}, \tag{16}$$

for boundary operator $\mathbf{B} : \partial\Omega \to \mathbb{C}^{q,q}$ and field $\mathbf{y}_{BC} \in \left[\mathrm{L}^2(\partial\Omega)\right]^q$, which finally leads to the frequency problem:

Problem 1.6 (p-dimensional time-harmonic hyperbolic problem)**.** Find $\mathbf{y} \in \left[\mathrm{L}^2(\Omega)\right]^q$ such that we have

$$\begin{cases} i\kappa\mathbf{M}\mathbf{y} + \displaystyle\sum_{j=1}^{p} \frac{\partial \boldsymbol{\phi}^j}{\partial x_j} = \boldsymbol{\psi} & \text{in } \Omega \qquad \text{with} \quad \boldsymbol{\phi}^j = \mathbf{F}^j\mathbf{y}, \quad \forall\, j \in [\![1,p]\!], \\ \mathbf{B}\mathbf{y} = \mathbf{B}\mathbf{y}_{BC} & \text{on } \partial\Omega. \end{cases} \tag{17}$$

Remark 1.7. We highlight the fact this part does not aim at giving general conditions on $\mathbf{M}$, $(\mathbf{F}^j)_{j\in[\![1,p]\!]}$ and $\mathbf{B}$ to ensure the well-posedness of Problem 1.6 (even if it has specifically been done for both Problems 1.1 and 1.4). This general presentation presupposes they are all given (as well as flux correction polynomial functions and a numerical trace computation definition, as detailed in Subsection 2.3), and it will introduce the associated FR formulation.

1.3. **Admissible boundary conditions through flux operator decomposition**

In this subsection, we precise some generic boundary conditions leading to a uniquely solvable Problem 1.6.

Definition 1.8. For a boundary face of normal $\mathbf{n}_{\partial\Omega}$, let's introduce a symmetric positive definite surface metric $\widetilde{\mathbf{M}} \in \mathbb{R}^{q,q}$ and consider the generalised eigenvalue problem

$$\mathbf{F}[\mathbf{n}_{\partial\Omega}]\mathbf{w} = \lambda\widetilde{\mathbf{M}}\mathbf{w}, \tag{18}$$

where we recall that $\mathbf{F}[\boldsymbol{\xi}] = \xi_1\mathbf{F}^1 + \cdots + \xi_p\mathbf{F}^p$ for any $\boldsymbol{\xi} \in \mathbb{R}^p$. This leads to the decomposition

$$\mathbf{F}[\mathbf{n}_{\partial\Omega}] = \widetilde{\mathbf{M}}\mathbf{P}\boldsymbol{\Lambda}\mathbf{P}^{-1}, \tag{19}$$

for a real diagonal matrix $\boldsymbol{\Lambda} \in \mathbb{R}^{q,q}$ of eigenvalues, and a matrix $\mathbf{P} \in \mathbb{R}^{q,q}$ of eigenvector coordinates.
Then, we can introduce the decomposition of $\mathbf{F}[\mathbf{n}_{\partial\Omega}]$ into positive and negative parts as

$$\mathbf{F}[\mathbf{n}_{\partial\Omega}] = \mathbf{F}^{\rightarrow}_{\widetilde{\mathbf{M}}}[\mathbf{n}_{\partial\Omega}] + \mathbf{F}^{\leftarrow}_{\widetilde{\mathbf{M}}}[\mathbf{n}_{\partial\Omega}] \quad \text{with} \quad \mathbf{F}^{\rightarrow}_{\widetilde{\mathbf{M}}}[\mathbf{n}_{\partial\Omega}] = \widetilde{\mathbf{M}}\mathbf{P}\boldsymbol{\Lambda}^{+}\mathbf{P}^{-1} \quad \text{and} \quad \mathbf{F}^{\leftarrow}_{\widetilde{\mathbf{M}}}[\mathbf{n}_{\partial\Omega}] = \widetilde{\mathbf{M}}\mathbf{P}\boldsymbol{\Lambda}^{-}\mathbf{P}^{-1}, \tag{20}$$

where $\boldsymbol{\Lambda}^{+}$ (respectively $\boldsymbol{\Lambda}^{-}$) denotes the positive (respectively strictly negative) part of $\boldsymbol{\Lambda}$.

Thus, most of the BCs can be written in terms of the incoming flux as

$$\mathbf{B}\mathbf{y} = \mathbf{F}^{\leftarrow}_{\widetilde{\mathbf{M}}}[\mathbf{n}_{\partial\Omega}]\mathbf{y} = \mathbf{B}\mathbf{y}_{BC}, \tag{21}$$

which will be illustrated in Section 3 for our two model problems.

Remark 1.9. In particular, the definition $\mathbf{B} = \mathbf{F}^{\leftarrow}_{\widetilde{\mathbf{M}}}[\mathbf{n}_{\partial\Omega}]$ falls within the framework of the admissible BCs for Friedrichs systems [11, 13], and it is possible to show the solution uniqueness of the associated Problem 1.6 by leaning on the unique continuation theorem.

2. FR Method principle: a strong polynomial PDE

After defining the general hyperbolic framework, one naturally would like to introduce the discrete counterpart of (17). The approximations $\mathbf{y}_\mathbf{h}$ and $\boldsymbol{\phi}^j_\mathbf{h}$ of the primal and dual variables are then defined, for a given mesh, by:
Find $\mathbf{y}_\mathbf{h} \in \boldsymbol{\mathcal{V}}_{\mathbf{h},\mathbf{k}}$ such that we have in every cell of the mesh

$$i\kappa\mathbf{M}\mathbf{y}_\mathbf{h} + \sum_{j=1}^{p} \frac{\partial \boldsymbol{\phi}^j_\mathbf{h}}{\partial x_j} = \boldsymbol{\psi}_\mathbf{h} \quad \text{with} \quad \boldsymbol{\phi}^j_\mathbf{h} = \mathbf{F}^j\mathbf{y}_\mathbf{h}, \quad \forall\, j \in [\![1, p]\!], \tag{22}$$

where $\boldsymbol{\mathcal{V}}_{\mathbf{h},\mathbf{k}}$ stands for a piecewise discontinuous polynomial function space defined on the mesh, and $\boldsymbol{\psi}_\mathbf{h}$ is a piecewise polynomial approximation of the RHS $\boldsymbol{\psi}$. This formulation is unfortunately ill-posed since it contains neither information on the solution continuity nor the boundary conditions.
The idea of the FR method (as initially introduced by Huynh [20]) is to introduce a non-trivial extension $\widetilde{\mathbf{F}}^j$ of the flux operator $\mathbf{F}^j$ to piecewise polynomial functions. This leads to the FR formulation:

Problem 2.1 (Discrete problem)**.** Find $\mathbf{y}_\mathbf{h} \in \boldsymbol{\mathcal{V}}_{\mathbf{h},\mathbf{k}}$ such that we have in every cell of the mesh

$$i\kappa\mathbf{M}\mathbf{y}_\mathbf{h} + \sum_{j=1}^{p} \frac{\partial \widetilde{\boldsymbol{\phi}}^j_\mathbf{h}}{\partial x_j} = \boldsymbol{\psi}_\mathbf{h} \quad \text{with} \quad \widetilde{\boldsymbol{\phi}}^j_\mathbf{h} = \widetilde{\mathbf{F}}^j\mathbf{y}_\mathbf{h} \quad \forall\, j \in [\![1, p]\!]. \tag{23}$$

Thus, this section is devoted to the introduction of the mesh, the approximation space $\boldsymbol{\mathcal{V}}_{\mathbf{h},\mathbf{k}}$ and the flux operator extension $\widetilde{\mathbf{F}}^j$.

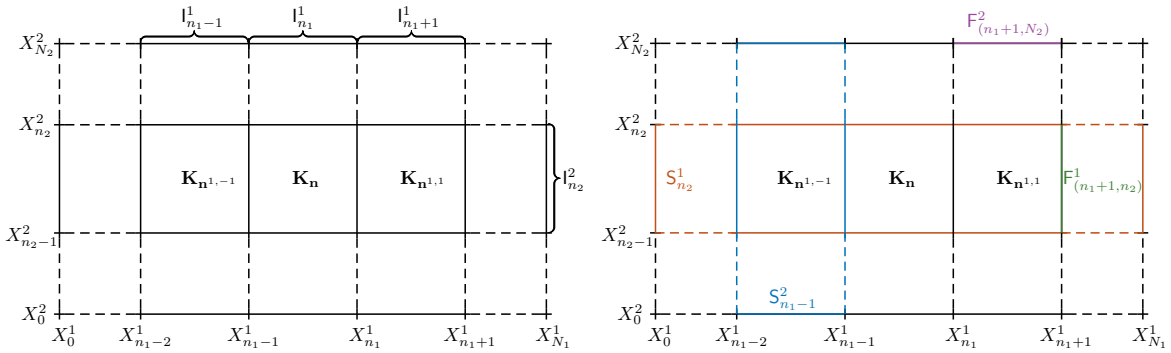

(I) Main mesh characteristics (II) Faces and strips

FIGURE 1. Mesh introduction in the case $p = 2$.

2.1. **Mesh characterisation**

We introduce a p-hyperrectangular domain $\Omega \subset \mathbb{R}^p$ and a direction-wise uniform mesh (see Figure 1i) whose cells $\mathbf{K}_\mathbf{n}$ are numbered by a multiindex $\mathbf{n} = (n_j)_{j\in[\![1,p]\!]} \in \mathcal{N}$ with

$$\Omega = \prod_{j=1}^{p}[0, L_j], \quad \mathbf{K}_\mathbf{n} = \prod_{j=1}^{p} \mathsf{I}^j_{n_j}, \quad \mathcal{N} = \prod_{j=1}^{p}[\![1, N_j]\!], \quad \mathsf{I}^j_{n_j} = [X^j_{n_j-1}, X^j_{n_j}], \quad X^j_n = nh_j, \quad h_j = \frac{L_j}{N_j}. \tag{24}$$

Definition 2.2. We introduce the set $\mathcal{F}^j = \left(\mathsf{F}^j_{\mathbf{n}^F}\right)_{\mathbf{n}^F\in\mathcal{N}^j_F}$ of faces which are orthogonal to $\mathbf{e}_j$ (see Figure 1ii)

$$\mathsf{F}^j_{\mathbf{n}^F} = \mathsf{I}^1_{n^F_1} \times \cdots \times \mathsf{I}^{j-1}_{n^F_{j-1}} \times \left\{X^j_{n^F_j}\right\} \times \mathsf{I}^{j+1}_{n^F_{j+1}} \times \cdots \times \mathsf{I}^p_{n^F_p}, \tag{25}$$

being numbered by $\mathbf{n}^F \in \mathcal{N}^j_F$ with

$$\mathcal{N}^j_F = [\![1, N_1]\!] \times \cdots \times [\![1, N_{j-1}]\!] \times [\![0, N_j]\!] \times [\![1, N_{j+1}]\!] \times \cdots \times [\![1, N_p]\!]. \tag{26}$$

Then, in order to shorten the notations, we also introduce dedicated notations to specific behaviours relative to a chosen direction $j \in [\![1, p]\!]$.

Definition 2.3 (Direction-wise notations)**.** For all $a, b \in \mathbb{N}^*$, $\mathbf{a}, \mathbf{b} \in [\mathbb{N}^*]^p$ and $\mathbf{x} = (x_1, \ldots, x_p) \in \mathbb{R}^p$, we denote

$$\begin{aligned} \mathbf{x}_{\setminus j} &= (x_1, \ldots, x_{j-1}, x_{j+1}, \ldots, x_p) \in \mathbb{R}^{p-1}, & [\![a, b]\!]_{\setminus j} &= [\![a, b]\!]\setminus\{j\}, \\ [\![\mathbf{a}, \mathbf{b}]\!] &= \prod_{j'\in[\![1,p]\!]} [\![a_{j'}, b_{j'}]\!] \subset \mathbb{N}^p, & \text{and} \quad [\![\mathbf{a}, \mathbf{b}]\!]_{\setminus j} &= \prod_{j'\in[\![1,p]\!]_{\setminus j}} [\![a_{j'}, b_{j'}]\!] \subset \mathbb{N}^{p-1}. \end{aligned} \tag{27}$$

Finally, the following definition makes it easy to refer to the cells adjacent to the one of interest.

Definition 2.4. For any $\mathbf{c} = (c_1, \ldots, c_p) \in \mathbb{N}^p$, let $\mathbf{c}^{j,\pm1}$ denote the shifted vector along direction j

$$\mathbf{c}^{j,\pm1} = (c_1, \ldots, c_{j-1}, c_j \pm 1, c_{j+1}, \ldots, c_p). \tag{28}$$

2.2. **Primal and dual variable approximations**

In this subsection, we define the function spaces for the approximation of the primal variable $\mathbf{y} \in \left[\mathrm{L}^2(\Omega)\right]^q$ and the dual variables $\boldsymbol{\phi}^j \in \left[\mathrm{L}^2(\Omega)\right]^q$ satisfying (17), i.e.

$$\sum_{j=1}^{p} \frac{\partial \boldsymbol{\phi}^j}{\partial x_j} = \boldsymbol{\psi} - i\kappa \mathbf{M}\mathbf{y} \in \left[\mathrm{L}^2(\Omega)\right]^q. \tag{29}$$

The primal variable $\mathbf{y}$ is approximated by a piecewise multivariate polynomial function $\mathbf{y_h} \in \boldsymbol{\mathcal{V}}_{\mathbf{h},\mathbf{k}}$.

Definition 2.5 (Primal approximation space)**.** We introduce the discrete primal approximation space (in 1 and q dimensions) of complex valued piecewise multivariate polynomial functions of degree at most $\mathbf{k} = (k_j)_{j\in[\![1,p]\!]} \in \mathbb{N}^p$ in each variable

$$\mathcal{V}_{\mathbf{h},\mathbf{k}} = \left\{ w \in \mathrm{L}^2(\Omega) \ : \ \forall\, \mathbf{n} \in \mathcal{N},\ w|_{\mathbf{K_n}} \in \mathcal{Q}_{\mathbf{k}}(\mathbf{K_n}) \right\} \quad \text{and} \quad \boldsymbol{\mathcal{V}}_{\mathbf{h},\mathbf{k}} = \left[\mathcal{V}_{\mathbf{h},\mathbf{k}}\right]^q, \tag{30}$$

where

$$\mathcal{Q}_{\mathbf{k}}(\mathbf{K_n}) = \left\{ w \in \mathrm{L}^2(\mathbf{K_n}) \ : \ w(\mathbf{x}) = \sum_{\mathbf{m}\in[\![\mathbf{0},\mathbf{k}]\!]} \alpha_{\mathbf{m}} \mathbf{x}^{\mathbf{m}},\ \alpha_{\mathbf{m}} \in \mathbb{C} \right\} \quad \text{with} \quad \mathbf{x}^{\mathbf{m}} = \prod_{j\in[\![1,p]\!]} (x_j)^{m_j}. \tag{31}$$

Definition 2.6. We also introduce the space $\mathrm{H}^1(\mathcal{T}_\mathbf{h})$ of piecewise H^1 functions on the mesh, which will give us a general framework for further estimates

$$\mathrm{H}^1(\mathcal{T}_\mathbf{h}) = \left\{ w \in \mathrm{L}^2(\Omega) \ : \ \forall\, \mathbf{n} \in \mathcal{N},\ w|_{\mathbf{K_n}} \in \mathrm{H}^1(\mathbf{K_n}) \right\}. \tag{32}$$

This allows, for any $\mathbf{n} \in \mathcal{N}$ and $\mathbf{w} \in \left[\mathrm{H}^1(\mathcal{T}_\mathbf{h})\right]^q$, to denote its restriction to $\mathbf{K_n}$ as $\mathbf{w_n} := \mathbf{w}|_{\mathbf{K_n}} \in \left[\mathrm{H}^1(\mathbf{K_n})\right]^q$.

Since $\displaystyle\sum_{j=1}^{p} \frac{\partial \boldsymbol{\phi}^j}{\partial x_j} \in \left[\mathrm{L}^2(\Omega)\right]^q$, it is natural to look for the dual variable approximation $\widetilde{\boldsymbol{\phi}}^j_\mathbf{h}$ as a continuous function in the direction $\mathbf{e}_j$. This introduces the space

$$\mathrm{C}^0_j(\Omega) = \left\{ w \in \mathrm{L}^2(\Omega) \ : \ \forall\, \mathbf{n}_{\backslash j} \in [\![\mathbf{1},\mathbf{N}]\!]_{\backslash j},\ w|_{\mathsf{S}^j_{\mathbf{n}_{\backslash j}}} \in \mathrm{C}^0\left(\mathsf{S}^j_{\mathbf{n}_{\backslash j}}\right) \right\} \tag{33}$$

of functions which are continuous on every strip $\mathsf{S}^j_{\mathbf{n}_{\backslash j}}$ of direction j defined by (see Figure 1ii)

$$\mathsf{S}^j_{\mathbf{n}_{\backslash j}} = \mathsf{I}^1_{n_1} \times \cdots \times \mathsf{I}^{j-1}_{n_{j-1}} \times [0, L_j] \times \mathsf{I}^{j+1}_{n_{j+1}} \times \cdots \times \mathsf{I}^p_{n_p}. \tag{34}$$

Thus, with the aim of having all the terms of (23) with the same polynomial degree, each dual variable $\boldsymbol{\phi}^j$ will be approximated by $\widetilde{\boldsymbol{\phi}}^j_\mathbf{h} \in \boldsymbol{\mathcal{W}}^j_{\mathbf{h},\mathbf{k}}$, with:

Definition 2.7 (Dual approximation spaces)**.** For a direction $j \in [\![1,p]\!]$, we introduce the discrete dual approximation space of complex valued piecewise multivariate polynomial functions of degree at most $\mathbf{k}^{j,1} \in \mathbb{N}^p$ in each variable, and continuous in direction $\mathbf{e}_j$

$$\boldsymbol{\mathcal{W}}^j_{\mathbf{h},\mathbf{k}} = \mathcal{V}_{\mathbf{h},\mathbf{k}^{j,1}} \cap \left[\mathrm{C}^0_j(\Omega)\right]^q \quad \text{with} \quad \mathbf{k}^{j,1} = (k_0, \ldots, k_{j-1}, k_j + 1, k_{j+1}, \ldots, k_p) \in \mathbb{N}^p. \tag{35}$$

Finally, the idea of the FR method is to approximate the solution (primal variable), the fluxes (dual variable) and the RHS by piecewise polynomials which solve the initial PDE on each cell $\mathbf{K_n}$, for $\mathbf{n} \in \mathcal{N}$

$$i\kappa \mathbf{M} \mathbf{y}_{\mathbf{h},\mathbf{n}} + \sum_{j=1}^{p} \frac{\partial \widetilde{\boldsymbol{\phi}}^j_{\mathbf{h},\mathbf{n}}}{\partial x_j} = \left(\Pi_{\mathbf{h},\mathbf{k}} \boldsymbol{\psi}\right)_{\mathbf{n}}, \tag{36}$$

where $\Pi_{\mathbf{h},\mathbf{k}} : \left[\mathrm{L}^2(\Omega)\right]^q \to \boldsymbol{\mathcal{V}}_{\mathbf{h},\mathbf{k}}$ denotes a projection from $\left[\mathrm{L}^2(\Omega)\right]^q$ to the discrete space $\boldsymbol{\mathcal{V}}_{\mathbf{h},\mathbf{k}}$, whose choice belongs to the user (such as the L^2-projection or an interpolation on a set of points for example).

2.3. **Local approximation of the fluxes**

The flux operator $\mathbf{F}^j$ is a local linear operator. It can naturally be extended to $\boldsymbol{\mathcal{V}}_{\mathbf{h},\mathbf{k}}$ and associates to the approximation $\mathbf{y_h}$ of the primal variable an approximation $\boldsymbol{\phi}^j_{\mathbf{h}}$ of the dual variable given by

$$\boldsymbol{\phi}^j_{\mathbf{h}} = \mathbf{F}^j \mathbf{y_h}. \tag{37}$$

Yet, the FR formulation relies on a nontrivial and nonlocal extension $\widetilde{\mathbf{F}}^j : \boldsymbol{\mathcal{V}}_{\mathbf{h},\mathbf{k}} \to \boldsymbol{\mathcal{W}}^j_{\mathbf{h},\mathbf{k}}$, $\mathbf{y_h} \mapsto \widetilde{\boldsymbol{\phi}}^j_{\mathbf{h}}$ of the flux operator $\mathbf{F}^j$ which is obtained by perturbing it as

$$\widetilde{\mathbf{F}}^j = \mathbf{F}^j + \delta \mathbf{F}^j. \tag{38}$$

through a polynomial correction of the flux $\boldsymbol{\phi}^j_{\mathbf{h}}$ at the interfaces which will be detailed in this Subsection.
Moreover, so as to ensure the consistency of the method, we will only consider perturbations which vanish for the exact solution, meaning that

$$\delta \mathbf{F}^j(\mathbf{y}) = \mathbf{0} \text{ for the exact solution } \mathbf{y}. \tag{39}$$

First, as $\mathbf{y_h}$ and $\boldsymbol{\phi}^j_{\mathbf{h}}$ may be discontinuous across interfaces, we need to introduce their 'direct' traces on any face from the neighbouring cells (two cells in the case of an internal interface, and one otherwise), as illustrated in Figure 2.

Definition 2.8 (Direct traces)**.** Let $\mathsf{F} \in \mathcal{F}^j$ be an internal face orthogonal to $\mathbf{e}_j$ such that $\mathsf{F} = \mathbf{K}_{\mathbf{n}^{j,-1}} \cap \mathbf{K}_{\mathbf{n}}$. The direct traces of $\mathbf{y_h}$ and $\boldsymbol{\phi}^j_{\mathbf{h}}$ on F (respectively 'just after' and 'just before' it) are defined by

$$\forall\, \mathbf{x} \in \mathsf{F},\ \begin{cases} \mathbf{y}^+_{\mathbf{h},\mathsf{F}}(\mathbf{x}_{\setminus j}) = \mathbf{y}_{\mathbf{h},\mathbf{n}}(\mathbf{x}) & \text{and} \quad \boldsymbol{\phi}^{j,+}_{\mathbf{h},\mathsf{F}} = \mathbf{F}^j\left[\mathbf{y}^+_{\mathbf{h},\mathsf{F}}\right], \\ \mathbf{y}^-_{\mathbf{h},\mathsf{F}}(\mathbf{x}_{\setminus j}) = \mathbf{y}_{\mathbf{h},\mathbf{n}^{j,-1}}(\mathbf{x}) & \text{and} \quad \boldsymbol{\phi}^{j,-}_{\mathbf{h},\mathsf{F}} = \mathbf{F}^j\left[\mathbf{y}^-_{\mathbf{h},\mathsf{F}}\right]. \end{cases} \tag{40}$$

In particular, $\mathbf{y}^{\pm}_{\mathbf{h},\mathsf{F}},\ \boldsymbol{\phi}^{j,\pm}_{\mathbf{h},\mathsf{F}} \in \left[\mathcal{Q}_{\mathbf{k}_{\setminus j}}(\mathsf{F})\right]^q$, and this definition naturally extends to boundary interfaces.

Then, as we want to impose the BCs and the continuity of the flux approximation along the interfaces, we introduce flux numerical traces on them: the flux on both sides of the faces will be corrected to fit with these values and thus be single-valued on these interfaces (as illustrated in Figure 2).
Therefore, Definitions 2.9 and 2.11 will introduce generic ways to define such flux numerical traces on internal and boundary faces, even if absolutely general methods could be used.

First, for an internal face $\mathsf{F} \in \mathcal{F}^j$, we presuppose the reader is able to give a decomposition of $\mathbf{F}^j$ that will divide the influence of both sides in terms of the flux numerical trace.

Definition 2.9 (Internal flux numerical traces)**.** Let $\mathsf{F} \in \mathcal{F}^j$ be an internal face orthogonal to $\mathbf{e}_j$. Assume the following decomposition of the directional flux operator: $\mathbf{F}^j = \mathbf{F}^{j,\rightarrow} + \mathbf{F}^{j,\leftarrow}$. The numerical trace $\gamma_{\mathsf{F}} \widetilde{\boldsymbol{\phi}}^j_{\mathbf{h}}$ of the

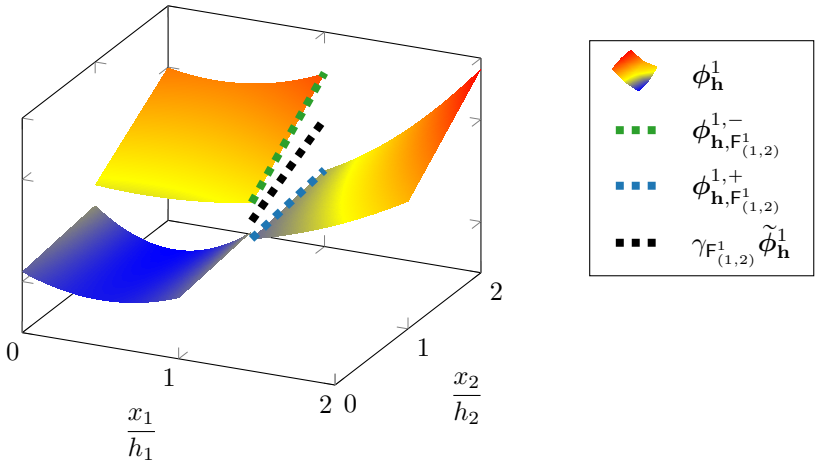

FIGURE 2. Illustration of the piecewise discontinuous flux in direction 1, $\boldsymbol{\phi}^1_{\mathbf{h}} = \mathbf{F}^1\mathbf{y}_{\mathbf{h}}$, with its direct and numerical traces, for $p = 2$ and $\mathbf{k} = (2, 1)$.

reconstructed flux $\widetilde{\boldsymbol{\phi}}^j_{\mathbf{h}}$ on F is defined by:

$$\gamma_{\mathsf{F}}\widetilde{\boldsymbol{\phi}}^j_{\mathbf{h}} = \mathbf{F}^{j,\rightarrow}\left[\mathbf{y}^-_{\mathbf{h},\mathsf{F}}\right] + \mathbf{F}^{j,\leftarrow}\left[\mathbf{y}^+_{\mathbf{h},\mathsf{F}}\right], \tag{41}$$

where $\mathbf{y}^{\pm}_{\mathbf{h},\mathsf{F}}$ were introduced in Definition 2.8. In particular, $\gamma_{\mathsf{F}}\widetilde{\boldsymbol{\phi}}^j_{\mathbf{h}} \in \left[\mathbb{Q}_{\mathbf{k}_{\setminus j}}(\mathsf{F})\right]^q$.

Remark 2.10. As detailed in Subsection 1.3 and illustrated in Section 3, such a decomposition can be obtained by solving a generalised eigenvalue problem for a given symmetric positive definite matrix $\widetilde{\mathbf{M}} \in \mathbb{R}^{q,q}$, taking $\mathbf{F}^{j,\rightarrow}$ and $\mathbf{F}^{j,\leftarrow}$ as the associated positive and negative parts of $\mathbf{F}^j$ (see [19] for example). Moreover, one classically makes the choice $\widetilde{\mathbf{M}} = \mathbf{M}$ for the internal interfaces.

In the same idea, such a numerical trace has to be defined on the boundary faces to take the BCs into account. To do so, we presuppose the reader is able to express the incoming flux with respect to a given surface metric.

Definition 2.11 (Boundary flux numerical traces)**.** Let us consider a direction $j \in [\![1, p]\!]$, a boundary face $\mathsf{F} \in \mathcal{F}^j$ orthogonal to $\mathbf{e}_j$, with $\mathbf{n} \in \mathcal{N}$ the index of its neighbouring cell and $s \in [\![1, 2p]\!]$ the index of the corresponding boundary interface, such that $\mathsf{F} = \mathbf{K}_{\mathbf{n}} \cap \partial\Omega_s$.
Moreover, we denote the incoming and outgoing directions as *id* and *od*, which stand for $\rightarrow$ and $\leftarrow$ (respectively $\leftarrow$ and $\rightarrow$) if $n_j = 1$ (respectively $n_j = N_j$). Furthermore, *is* stands for the internal side of the boundary, corresponding to $+$ (respectively $-$) if $n_j = 1$ (respectively $n_j = N_j$).
Finally, we suppose that, for this face F, we are given a decomposition of the directional flux operator $\mathbf{F}^j = \mathbf{F}^{j,\rightarrow} + \mathbf{F}^{j,\leftarrow}$, such that the BC can be written as

$$\mathbf{F}^{j,id}\mathbf{y} = \mathbf{g}^{\mathsf{F}} \quad \text{on } \mathsf{F}, \tag{42}$$

where $\mathbf{g}^{\mathsf{F}} : \mathsf{F} \rightarrow \mathrm{im}\,(\mathbf{F}^{j,id})$.
This allows to define a flux numerical trace polynomial $\gamma_{\mathsf{F}}\widetilde{\boldsymbol{\phi}}^j_{\mathbf{h}} \in \left[\mathcal{Q}_{\mathbf{k}_{\setminus j}}(\mathsf{F})\right]^q$ on F in the same way as (41), by replacing the incoming (and then undefined) component thanks to the previous expression:

$$\gamma_{\mathsf{F}}\widetilde{\boldsymbol{\phi}}^j_{\mathbf{h}} = \mathbf{F}^{j,od}\left[\mathbf{y}^{is}_{\mathbf{h},\mathsf{F}}\right] + \Pi^{\mathsf{F}}_{\mathbf{h},\mathbf{k}_{\setminus j}}\left[\mathbf{g}^{\mathsf{F}}\right], \tag{43}$$

where $\Pi^{\mathsf{F}}_{\mathbf{h},\mathbf{k}_{\setminus j}} : \left[\mathrm{L}^2(\mathsf{F})\right]^q \to \left[\mathbb{Q}_{\mathbf{k}_{\setminus j}}(\mathsf{F})\right]^q$ stands for a given projection on multivariate polynomial functions defined on F.

Remark 2.12. We highlight the fact that Definitions 2.9 and 2.11 offer specific ways to define the flux numerical traces in the consistency framework of (39): for both the equations of Subsection 1.1, their applications will be detailed in Section 3. Yet, they are not the only consistent possibilities, let alone the only choice to define a FR method.
Indeed, one may choose completely general ways to define $\gamma_{\mathsf{F}}\widetilde{\boldsymbol{\phi}}^j_{\mathbf{h}}$ on internal and boundary faces (not even ensuring consistency), and Definition 2.13 will still allow to define the associated FR formulation.
Finally, in any case, neither well-posedness nor convergence properties of the FR method are naturally ensured: this paper will prove them only for the specific Problem 4.4, and it is not destined to characterise a class of flux numerical traces that should be used for a general problem.

This finally allows to define the flux approximation $\widetilde{\boldsymbol{\phi}}^j_{\mathbf{h}}$. To do so, we impose the flux numerical traces at each interface thanks to flux correction polynomial functions of degree k_j+1: this will satisfy the expected continuity and polynomial degree properties.

Definition 2.13 (Flux approximation)**.** For $j \in [\![1,p]\!]$, let's introduce two polynomials $P^{j,\rightarrow}, P^{j,\leftarrow} \in \mathcal{Q}_{k_j+1}([0,1])$ such that

$$\left\{\begin{array}{rclcrcl} P^{j,\rightarrow}(0) & = & 1, & & P^{j,\rightarrow}(1) & = & 0, \\ P^{j,\leftarrow}(0) & = & 0, & & P^{j,\leftarrow}(1) & = & 1. \end{array}\right. \tag{44}$$

We define $\widetilde{\boldsymbol{\phi}}^j_{\mathbf{h}}$ as the perturbation of $\boldsymbol{\phi}^j_{\mathbf{h}} = \mathbf{F}^j\mathbf{y}_{\mathbf{h}} \in \boldsymbol{\mathcal{V}}_{\mathbf{h},\mathbf{k}}$ whose values at any interface $\mathsf{F} \in \mathcal{F}^j$ of normal $\mathbf{e}_j$ match the numerical trace polynomial functions $\gamma_{\mathsf{F}}\widetilde{\boldsymbol{\phi}}^j_{\mathbf{h}}$, thanks to corrections realised by $P^{j,\rightarrow}$ and $P^{j,\leftarrow}$.
More precisely, let's consider a cell $\mathbf{n} \in \mathcal{N}$ and its two faces along $\mathbf{e}_j$, respectively $\mathsf{F}^+ = \mathsf{F}^j_{\mathbf{n}^{j,-1}}$ and $\mathsf{F}^- = \mathsf{F}^j_{\mathbf{n}}$ on the 'left' and 'right' (in the j-th direction). Thus, we define $\widetilde{\boldsymbol{\phi}}^j_{\mathbf{h},\mathbf{n}}$ as

$$\forall\, \mathbf{x} \in \mathbf{K}_{\mathbf{n}},\ \widetilde{\boldsymbol{\phi}}^j_{\mathbf{h},\mathbf{n}}(\mathbf{x}) = \boldsymbol{\phi}^j_{\mathbf{h},\mathbf{n}}(\mathbf{x}) + \boldsymbol{\delta}^{\rightarrow}_{\mathbf{h},\mathsf{F}^+}(\mathbf{x}) + \boldsymbol{\delta}^{\leftarrow}_{\mathbf{h},\mathsf{F}^-}(\mathbf{x}), \tag{45}$$

where the perturbations from the 'left' and 'right' interfaces (in the j-th direction) are respectively

$$\boldsymbol{\delta}^{\rightarrow}_{\mathbf{h},\mathsf{F}^+}(\mathbf{x}) = \left(\gamma_{\mathsf{F}^+}\widetilde{\boldsymbol{\phi}}^j_{\mathbf{h}} - \boldsymbol{\phi}^{j,+}_{\mathbf{h},\mathsf{F}^+}\right)(\mathbf{x}_{\setminus j})\ P^{j,\rightarrow}(\widehat{x}_j) \quad \text{and} \quad \boldsymbol{\delta}^{\leftarrow}_{\mathbf{h},\mathsf{F}^-}(\mathbf{x}) = \left(\gamma_{\mathsf{F}^-}\widetilde{\boldsymbol{\phi}}^j_{\mathbf{h}} - \boldsymbol{\phi}^{j,-}_{\mathbf{h},\mathsf{F}^-}\right)(\mathbf{x}_{\setminus j})\ P^{j,\leftarrow}(\widehat{x}_j), \tag{46}$$

where $x_j = X^j_{n_j-1} + h_j\widehat{x}_j$ (see Figure 3).

Remark 2.14. One will observe that Definition 2.13 naturally ensures the increase to k_j+1 of the flux polynomial degree with respect to x_j, in addition to the continuity with respect to the j-th component (as the values at the interfaces of normal $\mathbf{e}_j$ are then single-valued with the numerical trace polynomials):

$$\forall\, \mathbf{n}^F \in \mathcal{N}^j_F,\ \forall\, \mathbf{x} \in \mathsf{F}^j_{\mathbf{n}^F},\ \widetilde{\boldsymbol{\phi}}^j_{\mathbf{h},\mathbf{n}^F}(\mathbf{x}) = \widetilde{\boldsymbol{\phi}}^j_{\mathbf{h},(\mathbf{n}^F)^{j,1}}(\mathbf{x}) = \gamma_{\mathsf{F}^j_{\mathbf{n}^F}}\widetilde{\boldsymbol{\phi}}^j_{\mathbf{h}}(\mathbf{x}_{\setminus j}). \tag{47}$$

This allows to complete the introduction of the Flux Reconstruction method with the strong polynomial equation (36), the flux numerical traces $\gamma_{\mathsf{F}}\widetilde{\boldsymbol{\phi}}^j_{\mathbf{h}}$ definition (with the examples of Definitions 2.9 and 2.11, or a general choice) and the flux approximation Definition 2.13: in any cell $\mathbf{K}_{\mathbf{n}}$, with $\mathbf{n} \in \mathcal{N}$, we get

$$i\kappa\mathbf{M}\mathbf{y}_{\mathbf{h},\mathbf{n}} + \sum_{j=1}^{p} \frac{\partial \widetilde{\boldsymbol{\phi}}^j_{\mathbf{h},\mathbf{n}}}{\partial x_j} = (\Pi_{\mathbf{h},\mathbf{k}}\boldsymbol{\psi})_{\mathbf{n}} \quad \text{with} \quad \widetilde{\boldsymbol{\phi}}^j_{\mathbf{h},\mathbf{n}} = \boldsymbol{\phi}^j_{\mathbf{h},\mathbf{n}} + \boldsymbol{\delta}^{\rightarrow}_{\mathbf{h},\mathsf{F}^j_{\mathbf{n}^{j,-1}}} + \boldsymbol{\delta}^{\leftarrow}_{\mathbf{h},\mathsf{F}^j_{\mathbf{n}}}. \tag{48}$$

Remark 2.15. We highlight the fact we did not introduce any set of solution points, as it is used to being done in classic definitions of the FR method (see [20, 44]). Such nodes are usually used as collocation points,

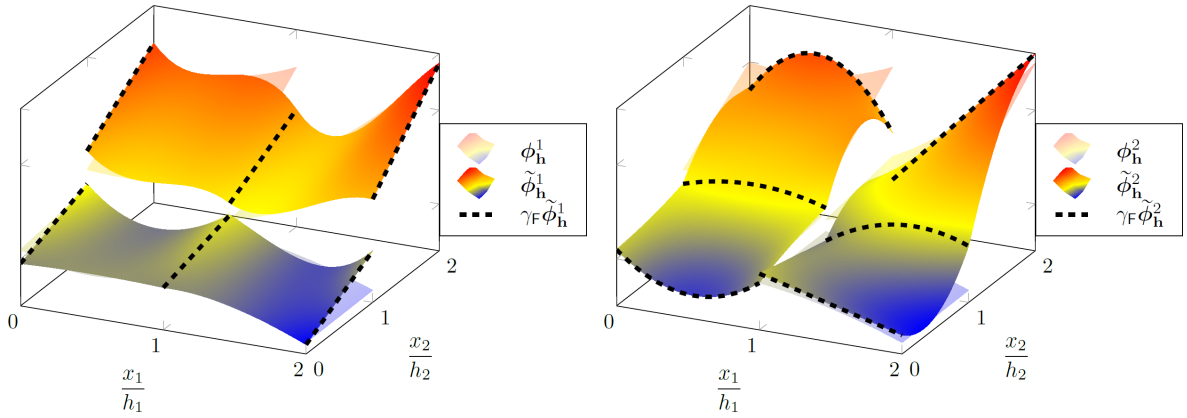

(I) Flux correction in direction 1 (II) Flux correction in direction 2

FIGURE 3. Illustration, for $p = 2$ and $\mathbf{k} = (2, 1)$, of the flux correction with the numerical traces, with respect to direct flux approximation: $\widetilde{\boldsymbol{\phi}}^1_{\mathbf{h}} \in \boldsymbol{\mathcal{V}}_{\mathbf{h},(3,1)}$ and $\widetilde{\boldsymbol{\phi}}^2_{\mathbf{h}} \in \boldsymbol{\mathcal{V}}_{\mathbf{h},(2,2)}$.

where the polynomial equation (48) is evaluated: the approximate solution is then reconstructed thanks to Lagrange polynomials. Yet, in this linear case, it has been shown thewe solution nodes have no influence on the method [20, 41] (without paying attention to the RHS projection which may depend on it, especially in case of interpolation), which avoids their introduction and additional notations.

Remark 2.16. The Spectral Difference (SD) method can be seen as a specific case of the FR approach **in this linear framework** [20]. Indeed, for each direction j, let's consider a set of $k_j + 2$ distinct flux points $\{\widehat{x}^{F,j}_0, \dots, \widehat{x}^{F,j}_{k_j+1}\} \subset [0, 1]$ such that $\widehat{x}^{F,j}_0 = 0$ and $\widehat{x}^{F,j}_{k_j+1} = 1$, with the associated Lagrange polynomials $\left(\mathcal{L}^{F,j}_l\right)_{l\in[\![0,k_j+1]\!]}$. Thus, by considering the specific flux correction polynomials

$$P^{j,\rightarrow} = \mathcal{L}^{F,j}_0 \quad \text{and} \quad P^{j,\leftarrow} = \mathcal{L}^{F,j}_{k_j+1}, \tag{49}$$

the associated FR formulation allows to retrieve the SD one. Similarly to Remark 2.15, SD definitions (see [24, 26]) rely on sets of solution points which have no influence in this linear case: they are only introduced as collocation points for the numerical implementation.
Equivalently, in this case, $\widetilde{\boldsymbol{\phi}}^j_{\mathbf{h}}$ can be defined as the unique element of $\boldsymbol{\mathcal{V}}_{\mathbf{h},\mathbf{k}^{j,1}}$ such that its restriction $\widetilde{\boldsymbol{\phi}}^j_{\mathbf{h},\mathbf{n}}$ to any $\mathbf{K}_{\mathbf{n}}$ is equal to:

- $\gamma_{\mathsf{F}^j_{\mathbf{n}^{j,-1}}}\widetilde{\boldsymbol{\phi}}^j_{\mathbf{h}}$ on $\mathsf{F}^j_{\mathbf{n}^{j,-1}}$ (the 'left' interface in the j-th direction).
- $\boldsymbol{\phi}^j_{\mathbf{h}}$ on the internal faces of the cell associated to the flux points, defined by

$$\left(\mathsf{I}^1_{n_1} \times \cdots \times \mathsf{I}^{j-1}_{n_{j-1}} \times \left\{h_j\left(n_j - 1 + \widehat{x}^{j,F}_l\right)\right\} \times \mathsf{I}^{j+1}_{n_{j+1}} \times \cdots \times \mathsf{I}^p_{n_p}\right)_{l\in[\![1,k_j]\!]}. \tag{50}$$

- $\gamma_{\mathsf{F}^j_{\mathbf{n}}}\widetilde{\boldsymbol{\phi}}^j_{\mathbf{h}}$ on $\mathsf{F}^j_{\mathbf{n}}$ (the 'right' interface in the j-th direction).

3. Application of the FR approach to the problems of interest

We will then specify the applications of Definitions 2.9 and 2.11 to the Problems 1.1 and 1.4: this will allow to characterise the FR methods we introduce for them.

3.1. **The FR formulation for the 1D wave equations**

Note 3.1. In the case of a single dimension, we will abandon the superscript of the direction j and the faces, reduced to a single point, will directly be referred as their number $n^F \in [\![0, N]\!]$ (see (51)). Moreover, as the cells K_n and intervals I_n are identical, we will only refer to I_n in this Subsection.

We take back Problem 1.1. Then, giving the set of numerical traces at the interfaces

$$\left(\gamma_{n^F}\widetilde{\boldsymbol{\phi}}_h\right)_{n^F\in[\![0,N]\!]}, \tag{51}$$

the corrected flux (see (45) and (46)) can be expressed on any I_n, for $n \in [\![1, N]\!]$, as

$$\widetilde{\boldsymbol{\phi}}_{h,n} = \boldsymbol{\phi}_{h,n} + \left(\gamma_{n-1}\widetilde{\boldsymbol{\phi}}_h - \boldsymbol{\phi}_{h,n}(X_{n-1})\right)\ P_n^{\rightarrow} + \left(\gamma_n\widetilde{\boldsymbol{\phi}}_h - \boldsymbol{\phi}_{h,n}(X_n)\right)\ P_n^{\leftarrow}, \tag{52}$$

where $P_n^{\rightarrow}$ and $P_n^{\leftarrow}$ stand for the transported versions of the flux correction polynomial functions on I_n:

$$\forall\ x \in \mathsf{I}_n, \quad P_n^{\rightarrow}(x) = P^{\rightarrow}(\widehat{x}) \quad \text{and} \quad P_n^{\leftarrow}(x) = P^{\leftarrow}(\widehat{x}) \quad \text{where} \quad x = X_{n-1} + h\widehat{x}. \tag{53}$$

Then, the last thing we need to completely define the FR method is the computation of these numerical traces. To do so, as mentioned in Remark 2.10, let's diagonalize the flux operator $\mathbf{F}$ with respect to $\mathbf{M} = \mathbf{I}_2$:

$$\mathbf{F} = \mathbf{P}\boldsymbol{\Lambda}\mathbf{P}^{-1} \quad \text{with} \quad \mathbf{P} = \begin{pmatrix} 1 & -1 \\ 1 & 1 \end{pmatrix} \quad \text{and} \quad \boldsymbol{\Lambda} = \begin{pmatrix} -1 & 0 \\ 0 & 1 \end{pmatrix}. \tag{54}$$

Thus, we introduce the flux operator decomposition as the positive and negative parts of $\mathbf{F}$

$$\begin{cases} \mathbf{F}^{\rightarrow} = \mathbf{P}\boldsymbol{\Lambda}^{+}\mathbf{P}^{-1} = \dfrac{1}{2}\begin{pmatrix} 1 & -1 \\ -1 & 1 \end{pmatrix} \quad \text{with} \quad \boldsymbol{\Lambda}^{+} = \begin{pmatrix} 0 & 0 \\ 0 & 1 \end{pmatrix}, \\ \mathbf{F}^{\leftarrow} = \mathbf{P}\boldsymbol{\Lambda}^{-}\mathbf{P}^{-1} = \dfrac{1}{2}\begin{pmatrix} -1 & -1 \\ -1 & -1 \end{pmatrix} \quad \text{with} \quad \boldsymbol{\Lambda}^{-} = \begin{pmatrix} -1 & 0 \\ 0 & 0 \end{pmatrix}, \end{cases} \tag{55}$$

which allows to define the flux numerical traces for internal faces according to Definition 2.9.
Concerning the boundaries, we refer to Subsection 1.3: we will highlight a surface metric $\widetilde{\mathbf{M}}$ whose associated decomposition of the flux operator $\mathbf{F}$ encompasses the BCs (2). Indeed, one has, for given complex values $Z_0 \neq 0$ and $Y_0 = (Z_0)^{-1} \neq 0$:

$$\mathbf{F} = \widetilde{\mathbf{M}}\mathbf{Q}\boldsymbol{\Lambda}\mathbf{Q}^{-1} \quad \text{with} \quad \widetilde{\mathbf{M}} = \begin{pmatrix} Y_0 & 0 \\ 0 & Z_0 \end{pmatrix} \quad \text{and} \quad \mathbf{Q} = \begin{pmatrix} (Z_0)^{1/2} & -(Z_0)^{1/2} \\ (Y_0)^{1/2} & (Y_0)^{1/2} \end{pmatrix}, \tag{56}$$

which allows to introduce

$$\mathbf{F}^{\rightarrow}_{\widetilde{\mathbf{M}}} = \widetilde{\mathbf{M}}\mathbf{Q}\boldsymbol{\Lambda}^{+}\mathbf{Q}^{-1} = \frac{1}{2}\begin{pmatrix} Y_0 & -1 \\ -1 & Z_0 \end{pmatrix} \quad \text{and} \quad \mathbf{F}^{\leftarrow}_{\widetilde{\mathbf{M}}} = \widetilde{\mathbf{M}}\mathbf{Q}\boldsymbol{\Lambda}^{-}\mathbf{Q}^{-1} = \frac{1}{2}\begin{pmatrix} -Y_0 & -1 \\ -1 & -Z_0 \end{pmatrix}. \tag{57}$$

Then, replacing (Z_0, Y_0) by (Z_1, Y_1) and (Z_2, Y_2) for the left and right boundaries respectively (and denoting the associated surface metrics as $\widetilde{\mathbf{M}}_1$ and $\widetilde{\mathbf{M}}_2$) that we suppose to be non-zero, one has

$$\begin{cases} \mathbf{F}^{\rightarrow}_{\widetilde{\mathbf{M}}_1}\mathbf{y}(0) = \dfrac{g_1}{2}\begin{pmatrix} Y_1 \\ -1 \end{pmatrix} \iff \begin{pmatrix} Y_1[u(0) - Z_1 v(0) - g_1] \\ -[u(0) - Z_1 v(0) - g_1] \end{pmatrix} = \mathbf{0} \iff u(0) - Z_1 v(0) = g_1, \\ \mathbf{F}^{\leftarrow}_{\widetilde{\mathbf{M}}_2}\mathbf{y}(L) = \dfrac{g_2}{2}\begin{pmatrix} -Y_2 \\ -1 \end{pmatrix} \iff \begin{pmatrix} -Y_2[u(L) + Z_2 v(L) - g_2] \\ -[u(L) + Z_2 v(L) - g_2] \end{pmatrix} = \mathbf{0} \iff u(L) + Z_2 v(L) = g_2. \end{cases} \tag{58}$$

Thus, the framework of Definition 2.11, with $\mathbf{F}^{\rightarrow}_{\widetilde{\mathbf{M}}_1}$, $\mathbf{F}^{\leftarrow}_{\widetilde{\mathbf{M}}_2}$ and (58), allows to take the BCs into account, and then defines an associated numerical trace.

Remark 3.2 (BCs for Dirichlet and Neumann conditions)**.** Finally, one will note that the previous condition does not allow to take into account Dirichlet ($Z_0 = 0$) and Neumann ($Y_0 = 0$) conditions. To solve this limitation, let's first highlight that (55) leads, on the left and right boundaries respectively, to

$$\left\{\begin{array}{rcl} \mathbf{F}^{\rightarrow}_{\widetilde{\mathbf{M}}_1} & = & \frac{1}{2}\left[\begin{pmatrix} 1+Y_1 & 0 \\ 0 & 1+Z_1 \end{pmatrix}\mathbf{F}^{\rightarrow} \quad + \quad \begin{pmatrix} 1-Y_1 & 0 \\ 0 & 1-Z_1 \end{pmatrix}\mathbf{F}^{\leftarrow}\right], \\ \mathbf{F}^{\leftarrow}_{\widetilde{\mathbf{M}}_2} & = & \frac{1}{2}\left[\begin{pmatrix} 1-Y_2 & 0 \\ 0 & 1-Z_2 \end{pmatrix}\mathbf{F}^{\rightarrow} \quad + \quad \begin{pmatrix} 1+Y_2 & 0 \\ 0 & 1+Z_2 \end{pmatrix}\mathbf{F}^{\leftarrow}\right], \end{array}\right. \tag{59}$$

which allows to rewrite the BCs (58) as the expression of the incoming natural flux in terms of the reflection of the outgoing one:

$$\left\{\begin{array}{l} \mathbf{F}^{\rightarrow}\mathbf{y}(0) = \mathbf{R}^{\hookrightarrow}\mathbf{F}^{\leftarrow}\mathbf{y}(0) + \mathbf{G}_1 \quad \text{with} \quad \mathbf{G}_1 = \frac{g_1}{Z_1+1}\begin{pmatrix} 1 \\ -1 \end{pmatrix} \quad \text{and} \quad \mathbf{R}^{\hookrightarrow} = \begin{pmatrix} -R_1 & 0 \\ 0 & R_1 \end{pmatrix}, \\ \mathbf{F}^{\leftarrow}\mathbf{y}(L) = \mathbf{R}^{\hookleftarrow}\mathbf{F}^{\rightarrow}\mathbf{y}(L) + \mathbf{G}_2 \quad \text{with} \quad \mathbf{G}_2 = \frac{g_2}{Z_2+1}\begin{pmatrix} -1 \\ -1 \end{pmatrix} \quad \text{and} \quad \mathbf{R}^{\hookleftarrow} = \begin{pmatrix} -R_2 & 0 \\ 0 & R_2 \end{pmatrix}, \end{array}\right. \tag{60}$$

with $R_1 = \dfrac{Z_1 - 1}{Z_1 + 1}$ and $R_2 = \dfrac{Z_2 - 1}{Z_2 + 1}$ the classic expressions of the reflection coefficients at normal incidence. Moreover, replacing the undefined term of Definition 2.9 with these rewritings allows to define a numerical trace in more general conditions.

3.2. **The FR formulation for the 3D Maxwell problem**

In what follows, we suppose that ε_r and μ_r are constant in the whole domain (which is a subcase of the more general hypotheses of Problem 1.4).
In the framework of Subsection 2.3, we finally need to define the numerical traces. To do so, we consider the same mechanism as the one introduced in Subsection 3.1: the idea is to diagonalize each flux operator with respect to the scalar product induced by $\mathbf{M}$ (defined in (10)), before using their positive and negative parts as a decomposition. For example, we have $\mathbf{F}^x = \mathbf{M}\mathbf{P}^x\mathbf{\Lambda}^x(\mathbf{P}^x)^{-1}$, with

$$\mathbf{P}^x = \begin{pmatrix} 0 & 0 & 0 & 0 & 0 & (\varepsilon_r)^{-1/2} \\ -(\varepsilon_r)^{-1/2} & 0 & (\varepsilon_r)^{-1/2} & 0 & 0 & 0 \\ 0 & (\varepsilon_r)^{-1/2} & 0 & -(\varepsilon_r)^{-1/2} & 0 & 0 \\ 0 & 0 & 0 & 0 & (\mu_r)^{-1/2} & 0 \\ 0 & (\mu_r)^{-1/2} & 0 & (\mu_r)^{-1/2} & 0 & 0 \\ (\mu_r)^{-1/2} & 0 & (\mu_r)^{-1/2} & 0 & 0 & 0 \end{pmatrix} \text{ and } \mathbf{\Lambda}^x = \begin{pmatrix} -c\mathbf{I}_2 & \mathbf{0}_2 & \mathbf{0}_2 \\ \mathbf{0}_2 & c\mathbf{I}_2 & \mathbf{0}_2 \\ \mathbf{0}_2 & \mathbf{0}_2 & \mathbf{0}_2 \end{pmatrix} \tag{61}$$

where $\mathbf{\Lambda}^x$ is the diagonal matrix composed of the eigenvalues, while $\mathbf{P}^x$ is made of the eigenvector coordinates. The speed is also denoted as $c = \dfrac{1}{\sqrt{\varepsilon_r \mu_r}}$.
Thus, we introduce the flux operator decomposition $\mathbf{F}^x = \mathbf{F}^{x,\rightarrow} + \mathbf{F}^{x,\leftarrow}$ as its positive and negative parts.

This leads to $\mathbf{F}^{x,\rightarrow} = \mathbf{M}\mathbf{P}^x\mathbf{\Lambda}^{x,+}(\mathbf{P}^x)^{-1}$ and $\mathbf{F}^{x,\leftarrow} = \mathbf{M}\mathbf{P}^x\mathbf{\Lambda}^{x,-}(\mathbf{P}^x)^{-1}$ with

$$\left\{\begin{array}{rclcl} \mathbf{F}^{x,\rightarrow} & = & \mathbf{M}\mathbf{P}^x\mathbf{\Lambda}^{x,+}(\mathbf{P}^x)^{-1} & = & \dfrac{1}{2}\begin{pmatrix} Y\mathbf{\Gamma}_t[\mathbf{e}_x] & -\mathbf{\Gamma}_\times[\mathbf{e}_x] \\ \mathbf{\Gamma}_\times[\mathbf{e}_x] & Z\mathbf{\Gamma}_t[\mathbf{e}_x] \end{pmatrix} \quad \text{with} \quad \mathbf{\Lambda}^{x,+} = \begin{pmatrix} \mathbf{0}_2 & \mathbf{0}_2 & \mathbf{0}_2 \\ \mathbf{0}_2 & c\mathbf{I}_2 & \mathbf{0}_2 \\ \mathbf{0}_2 & \mathbf{0}_2 & \mathbf{0}_2 \end{pmatrix}, \\ \mathbf{F}^{x,\leftarrow} & = & \mathbf{M}\mathbf{P}^x\mathbf{\Lambda}^{x,-}(\mathbf{P}^x)^{-1} & = & \dfrac{1}{2}\begin{pmatrix} -Y\mathbf{\Gamma}_t[\mathbf{e}_x] & -\mathbf{\Gamma}_\times[\mathbf{e}_x] \\ \mathbf{\Gamma}_\times[\mathbf{e}_x] & -Z\mathbf{\Gamma}_t[\mathbf{e}_x] \end{pmatrix} \quad \text{with} \quad \mathbf{\Lambda}^{x,-} = \begin{pmatrix} -c\mathbf{I}_2 & \mathbf{0}_2 & \mathbf{0}_2 \\ \mathbf{0}_2 & \mathbf{0}_2 & \mathbf{0}_2 \\ \mathbf{0}_2 & \mathbf{0}_2 & \mathbf{0}_2 \end{pmatrix}, \end{array}\right. \tag{62}$$

where $Z = \sqrt{\dfrac{\mu_r}{\varepsilon_r}}$ and $Y = Z^{-1}$ stand for the internal impedance and admittance, and $\mathbf{\Gamma}_t[\mathbf{e}_x]$ and $\mathbf{\Gamma}_\times[\mathbf{e}_x]$ denote the matrices respectively associated to the operators $\gamma_t[\mathbf{e}_x]$ and $\gamma_\times[\mathbf{e}_x]$ (see (12)). This allows to define the flux numerical traces for internal faces according to Definition 2.9, in a similar way to classic ones [15, 29].
Then, for the boundaries, we introduce a surface metric $\widetilde{\mathbf{M}}$ whose associated decomposition will allow to take into account the BCs, as detailed in Subsection 1.3. Thus, for given values $Z_0 > 0$, $Y_0 = (Z_0)^{-1} > 0$ and the surface metric

$$\widetilde{\mathbf{M}} = \begin{pmatrix} ZY_0\varepsilon_r\mathbf{I}_3 & \mathbf{0}_3 \\ \mathbf{0}_3 & Z_0Y\mu_r\mathbf{I}_3 \end{pmatrix} \tag{63}$$

the generalised eigenvalue problem leads to the decomposition $\mathbf{F}^x = \mathbf{F}^{x,\rightarrow}_{\widetilde{\mathbf{M}}} + \mathbf{F}^{x,\leftarrow}_{\widetilde{\mathbf{M}}}$ with

$$\mathbf{F}^{x,\rightarrow}_{\widetilde{\mathbf{M}}} = \frac{1}{2}\begin{pmatrix} Y_0\mathbf{\Gamma}_t[\mathbf{e}_x] & -\mathbf{\Gamma}_\times[\mathbf{e}_x] \\ \mathbf{\Gamma}_\times[\mathbf{e}_x] & Z_0\mathbf{\Gamma}_t[\mathbf{e}_x] \end{pmatrix} \quad \text{and} \quad \mathbf{F}^{x,\leftarrow}_{\widetilde{\mathbf{M}}} = \frac{1}{2}\begin{pmatrix} -Y_0\mathbf{\Gamma}_t[\mathbf{e}_x] & -\mathbf{\Gamma}_\times[\mathbf{e}_x] \\ \mathbf{\Gamma}_\times[\mathbf{e}_x] & -Z_0\mathbf{\Gamma}_t[\mathbf{e}_x] \end{pmatrix}. \tag{64}$$

Then, considering left and right boundary faces of respective outgoing normals $\mathbf{n}_{\partial\Omega} = -\mathbf{e}_x$ and $\mathbf{n}_{\partial\Omega} = \mathbf{e}_x$, and their impedance $Z_{\partial\Omega}$ and admittance $Y_{\partial\Omega} = (Z_{\partial\Omega})^{-1}$ that we suppose strictly positive (with the associated surface metric $\widetilde{\mathbf{M}}_{\partial\Omega}$), one has

$$\left\{\begin{array}{lcl} \mathbf{F}^{\rightarrow}_{\widetilde{\mathbf{M}}_{\partial\Omega}}\mathbb{E} = \dfrac{1}{2}\begin{pmatrix} Y_{\partial\Omega}\mathbf{\Gamma}_t[-\mathbf{e}_x] \\ -\mathbf{\Gamma}_\times[-\mathbf{e}_x] \end{pmatrix}\mathbf{g} & \Longleftrightarrow & \gamma_t[-\mathbf{e}_x]\mathbf{e} + Z_{\partial\Omega}\gamma_\times[-\mathbf{e}_x]\mathbf{h} = \mathbf{g}, \\ \mathbf{F}^{\leftarrow}_{\widetilde{\mathbf{M}}_{\partial\Omega}}\mathbb{E} = \dfrac{1}{2}\begin{pmatrix} -Y_{\partial\Omega}\mathbf{\Gamma}_t[\mathbf{e}_x] \\ \mathbf{\Gamma}_\times[\mathbf{e}_x] \end{pmatrix}\mathbf{g} & \Longleftrightarrow & \gamma_t[\mathbf{e}_x]\mathbf{e} + Z_{\partial\Omega}\gamma_\times[\mathbf{e}_x]\mathbf{h} = \mathbf{g}, \end{array}\right. \tag{65}$$

where we use the fact that $\mathbf{g} \in \mathrm{L}^2_t(\partial\Omega)$ implies that $\mathbf{g} = \gamma_t[\mathbf{e}_x]\mathbf{g} = \gamma_t[-\mathbf{e}_x]\mathbf{g}$ on these boundary faces.
Thus, the framework of Definition 2.11 allows to take the BCs into account, and then defines an associated numerical trace. Similar considerations can be applied for the y and z axes.

Remark 3.3 (BCs for perfect conductor conditions)**.** Finally, one will note that the previous condition does not allow to take into account perfect electric ($Z_{\partial\Omega} = 0$) and magnetic ($Y_{\partial\Omega} = 0$) conductor conditions. To solve this limitation, let's first highlight that (62) leads, on left and right boundaries respectively, to

$$\left\{\begin{array}{rcl} \mathbf{F}^{x,\rightarrow}_{\widetilde{\mathbf{M}}_{\partial\Omega}} & = & \dfrac{1}{2}\left[\begin{pmatrix} 1+Y_{\partial\Omega}Z & 0 \\ 0 & 1+YZ_{\partial\Omega} \end{pmatrix}\mathbf{F}^{x,\rightarrow} + \begin{pmatrix} 1-Y_{\partial\Omega}Z & 0 \\ 0 & 1-YZ_{\partial\Omega}) \end{pmatrix}\mathbf{F}^{x,\leftarrow}\right], \\ \mathbf{F}^{x,\leftarrow}_{\widetilde{\mathbf{M}}_{\partial\Omega}} & = & \dfrac{1}{2}\left[\begin{pmatrix} 1-Y_{\partial\Omega}Z & 0 \\ 0 & 1-YZ_{\partial\Omega} \end{pmatrix}\mathbf{F}^{x,\rightarrow} + \begin{pmatrix} 1+Y_{\partial\Omega}Z & 0 \\ 0 & 1+YZ_{\partial\Omega} \end{pmatrix}\mathbf{F}^{x,\leftarrow}\right], \end{array}\right. \tag{66}$$

which allows to rewrite the BCs (65) as the expression of the incoming natural flux (associated to $\mathbf{M}$) in terms of the reflection of the outgoing one:

$$\begin{cases} \mathbf{F}^{x,\rightarrow}\mathbb{E} = \mathbf{R}^{\hookrightarrow}\mathbf{F}^{x,\leftarrow}\mathbb{E} + \mathbf{G}^{\hookrightarrow} \quad \text{with} \quad \mathbf{G}^{\hookrightarrow} = \dfrac{Z}{Z_{\partial\Omega}+Z}\begin{pmatrix} Y\mathbf{\Gamma}_t[-\mathbf{e}_x] \\ -\mathbf{\Gamma}_\times[-\mathbf{e}_x] \end{pmatrix}\mathbf{g} \quad \text{and} \quad \mathbf{R}^{\hookrightarrow} = \begin{pmatrix} -R\mathbf{I}_3 & \mathbf{0}_3 \\ \mathbf{0}_3 & R\mathbf{I}_3 \end{pmatrix}, \\ \mathbf{F}^{x,\leftarrow}\mathbb{E} = \mathbf{R}^{\hookleftarrow}\mathbf{F}^{x,\rightarrow}\mathbb{E} + \mathbf{G}^{\hookleftarrow} \quad \text{with} \quad \mathbf{G}^{\hookleftarrow} = \dfrac{Z}{Z_{\partial\Omega}+Z}\begin{pmatrix} -Y\mathbf{\Gamma}_t[\mathbf{e}_x] \\ \mathbf{\Gamma}_\times[\mathbf{e}_x] \end{pmatrix}\mathbf{g} \quad \text{and} \quad \mathbf{R}^{\hookleftarrow} = \begin{pmatrix} -R\mathbf{I}_3 & \mathbf{0}_3 \\ \mathbf{0}_3 & R\mathbf{I}_3 \end{pmatrix}, \end{cases} \tag{67}$$

with the classic expression of the reflection coefficient at normal incidence $R = \dfrac{Z_{\partial\Omega}-Z}{Z_{\partial\Omega}+Z}$. Moreover, replacing the undefined term of Definition 2.9 with these rewritings allows to define a numerical trace in more general conditions.

Remark 3.4. These numerical traces can also be obtained by considering a 1D Riemann solver or an upwinding mechanism (see respectively 2.3.2 and 2.3.3 from [39]). For the latter, the idea to look for the numerical trace as a linear combination of output traces from the neighbouring cells of the face (associating a virtual cell out of Ω in the boundary case).

4. A priori error estimates and well-posedness character

After detailing the construction of the Flux Reconstruction method, we focus on the homogeneous 1D time-harmonic wave Problem 4.4, with the numerical traces introduced in Subsection 3.1 and incoming BCs. Thus, this Section is devoted to show the well-posedness of the associated FR formulation, in addition to explicit a priori error estimates.

4.1. Main results

First, we detail the problem on which we focus, before summarising the main results.

Conjecture 4.1. For the rest of the paper, we assume the flux correction polynomials $P^{\rightarrow}$ and $P^{\leftarrow}$ are of degrees exactly $k+1$ and that the parameters are such that

$$\sum_{l=0}^{k+1} \left(P^{\rightarrow}\right)^{(l)}(0)\,(-i\kappa h)^{-l} \neq 0 \quad \text{and} \quad \sum_{l=0}^{k+1} \left(P^{\leftarrow}\right)^{(l)}(1)\,(i\kappa h)^{-l} \neq 0, \tag{68}$$

where $\left(P^{\rightarrow}\right)^{(l)}$ and $\left(P^{\leftarrow}\right)^{(l)}$ denote the l^{th} derivatives of $P^{\rightarrow}$ and $P^{\leftarrow}$ respectively.

Remark 4.2. We highlight the fact that:

1. For any given flux correction polynomial functions $P^{\rightarrow}$ and $P^{\leftarrow}$, by introducing the real polynomials of degrees $k+1$
$$T^{\rightarrow}(X) = \sum_{l=0}^{k+1} \left(P^{\rightarrow}\right)^{(l)}(0)\,X^l \quad \text{and} \quad T^{\leftarrow}(X) = \sum_{l=0}^{k+1} \left(P^{\leftarrow}\right)^{(l)}(1)\,X^l, \tag{69}$$
Conjecture 4.1 may be refuted for at most $\left\lfloor \dfrac{k+1}{2} \right\rfloor$ values of κh (which is the maximum number of their couples of non-zero conjugated purely imaginary roots).
2. Condition (68) is verified for h small enough, as $\left(P^{\rightarrow}\right)^{(k+1)}(0) \neq 0$ and $\left(P^{\leftarrow}\right)^{(k+1)}(1) \neq 0$.
3. All the numerical tests that we have implemented (for various flux correction polynomial functions, polynomial orders, domain lengths and wavenumbers) have verified this condition (see Subsection 5.1).

Claim 4.3. In what follows, we restrict the study to the homogeneous case $\boldsymbol{\psi} = (0,0)$ with the Boundary Conditions associated to $Z_1 = 1$ and $Z_2 = 1$, the numerical traces associated to (55) and (58), and flux correction polynomial functions of degrees exactly $k+1$ verifying Conjecture 4.1:

Problem 4.4. Find $\mathbf{y}_h = (u_h, v_h) \in \boldsymbol{\mathcal{V}}_{h,k}$ and $\widetilde{\boldsymbol{\phi}}_h \in \boldsymbol{\mathcal{W}}_{h,k}$ such that for all $n \in [\![1, N]\!]$

$$i\kappa \mathbf{y}_{h,n} + \frac{\mathrm{d}\widetilde{\boldsymbol{\phi}}_{h,n}}{\mathrm{d}x} = \mathbf{0} \quad \text{in } \mathsf{I}_n, \tag{70}$$

associated to the Boundary Conditions

$$\left\{ \begin{array}{rcrcl} u(X_0) & - & v(X_0) & = & g_1, \\ u(X_N) & + & v(X_N) & = & g_2, \end{array} \right. \tag{71}$$

and the flux numerical traces from Subsection 3.1.

Just before presenting the error estimates, we introduce two semi-norms for which they are developed.

Definition 4.5. For $w \in \mathrm{H}^1(\mathcal{T}_\mathbf{h})$ and $\mathbf{w} \in \left[\mathrm{H}^1(\mathcal{T}_\mathbf{h})\right]^2$ (see (32)), we define the semi-norms $|w|_\square$ and $|\mathbf{w}|_\square$ by

$$|w|_\square^2 = |w_1(X_0)|^2 + \sum_{n=1}^{N-1} |[\![w]\!]_n|^2 + |w_N(X_N)|^2 \quad \text{and} \quad |\mathbf{w}|_\square^2 = |\mathbf{w}_1(X_0)|^2 + \sum_{n=1}^{N-1} |[\![\mathbf{w}]\!]_n|^2 + |\mathbf{w}_N(X_N)|^2, \tag{72}$$

where we have denoted the modulus and the usual euclidean norm on $\mathbb{C}^2$ as $|\cdot|$ and the jumps of w and $\mathbf{w}$ as

$$\forall\, n \in [\![1, N-1]\!], \quad [\![w]\!]_n = w_{n+1}(X_n) - w_n(X_n) \quad \text{and} \quad [\![\mathbf{w}]\!]_n = \mathbf{w}_{n+1}(X_n) - \mathbf{w}_n(X_n). \tag{73}$$

Moreover, the semi-norms $|w|_{1,h}$ and $|\mathbf{w}|_{1,h}$ denote the broken H^1 semi-norms as

$$|w|_{1,h}^2 = \sum_{n=1}^{N} \int_{\mathsf{I}_n} |(w_n)^{(1)}(x)|^2 \,\mathrm{d}x \quad \text{and} \quad |\mathbf{w}|_{1,h}^2 = \sum_{n=1}^{N} \int_{\mathsf{I}_n} |(\mathbf{w}_n)^{(1)}(x)|^2 \,\mathrm{d}x. \tag{74}$$

Finally, we denote the L^2-norm on Ω as $\|w\|_0 = \|w\|_{\mathrm{L}^2(\Omega)}$ and $\|\mathbf{w}\|_0 = \|\mathbf{w}\|_{\mathrm{L}^2(\Omega)}$.

Thus, we can introduce the main result, which ensures the well-posedness of the FR approach, in addition to explicit asymptotic estimates of the error.

Theorem 4.6. *For κL fixed and κh verifying Conjecture* 4.1*, the Flux Reconstruction formulation associated to Problem* 4.4 *is well-posed.*
Moreover, for κh small enough, we have the following estimates of the error $\boldsymbol{\varepsilon}_h = \mathbf{y} - \mathbf{y}_h$ (for the norms introduced in Definition 4.5*):*

$$\begin{array}{lrcccl} (i) & |\boldsymbol{\varepsilon}_h|_\square^2 & \lesssim & & (\kappa L) & (\kappa h)^{2k+1} \quad \left(\mathsf{C}_\square^{\rightarrow} |g_1|^2 \,+\, \mathsf{C}_\square^{\leftarrow} |g_2|^2\right), \\ (ii) & \|\boldsymbol{\varepsilon}_h\|_0^2 & \lesssim & \kappa^{-1} & (\kappa L) & (\kappa h)^{2k+2} \quad \left(\mathsf{C}_{\mathrm{L}^2}^{\rightarrow} |g_1|^2 \,+\, \mathsf{C}_{\mathrm{L}^2}^{\leftarrow} |g_2|^2\right), \\ (iii) & |\boldsymbol{\varepsilon}_h|_{1,h}^2 & \lesssim & \kappa & (\kappa L) & (\kappa h)^{2k} \quad \left(\mathsf{C}_{\mathrm{H}^1}^{\rightarrow} |g_1|^2 \,+\, \mathsf{C}_{\mathrm{H}^1}^{\leftarrow} |g_2|^2\right), \end{array} \tag{75}$$

where the notation $A \lesssim B$ means that there exists a constant $C > 0$, independent of κ, h, k and L, such that we have $A \leqslant B\,C$. Moreover, we have the explicit expressions of the constants

$$\left\{\begin{array}{rcl} \mathsf{C}_{\square}^{\rightarrow} & = & \dfrac{1}{|T_{k+1}^{\rightarrow}|^2} \\ \mathsf{C}_{\square}^{\leftarrow} & = & \dfrac{1}{|T_{k+1}^{\leftarrow}|^2} \end{array}\right., \quad \left\{\begin{array}{rcl} \mathsf{C}_{\mathrm{L}^2}^{\rightarrow} & = & \dfrac{|B_k^{\rightarrow}|^2 + \frac{1}{3}(\kappa L)^2 |A_k^{\rightarrow}|^2}{|T_{k+1}^{\rightarrow}|^2} \\ \mathsf{C}_{\mathrm{L}^2}^{\leftarrow} & = & \dfrac{|B_k^{\leftarrow}|^2 + \frac{1}{3}(\kappa L)^2 |A_k^{\leftarrow}|^2}{|T_{k+1}^{\leftarrow}|^2} \end{array}\right. \quad \textit{and} \quad \left\{\begin{array}{rcl} \mathsf{C}_{\mathrm{H}^1}^{\rightarrow} & = & \dfrac{|C_k^{\rightarrow}|^2}{|T_{k+1}^{\rightarrow}|^2} \\ \mathsf{C}_{\mathrm{H}^1}^{\leftarrow} & = & \dfrac{|C_k^{\leftarrow}|^2}{|T_{k+1}^{\leftarrow}|^2} \end{array}\right., \tag{76}$$

which depend on

$$\left\{\begin{array}{rcl@{\quad}rcl} A_k^{\rightarrow} & = & \displaystyle\int_0^1 P^{\rightarrow}(\widehat{x})\ \mathrm{d}\widehat{x} & \textit{and} & A_k^{\leftarrow} & = & \displaystyle\int_0^1 P^{\leftarrow}(\widehat{x})\ \mathrm{d}\widehat{x}, \\ B_k^{\rightarrow} & = & \|P^{\rightarrow}\|_{\mathrm{L}^2(0,1)} & \textit{and} & B_k^{\leftarrow} & = & \|P^{\leftarrow}\|_{\mathrm{L}^2(0,1)}, \\ C_k^{\rightarrow} & = & \left\|(P^{\rightarrow})^{(1)}\right\|_{\mathrm{L}^2(0,1)} & \textit{and} & C_k^{\leftarrow} & = & \left\|(P^{\leftarrow})^{(1)}\right\|_{\mathrm{L}^2(0,1)}, \\ T_{k+1}^{\rightarrow} & = & (P^{\rightarrow})^{(k+1)}(0) & \textit{and} & T_{k+1}^{\leftarrow} & = & (P^{\leftarrow})^{(k+1)}(1). \end{array}\right. \tag{77}$$

Remark 4.7. One will note that Theorem 4.6 ensures quasi-optimal convergence orders, such as DG methods [10, 31] (as it will be highlighted in the numerical Section 5). In particular, this behaviour is allowed by the regularity of the exact solution $\mathbf{y}$ (see Remark 4.10). Moreover, the dependencies are explicit in terms of the flux correction polynomial functions, the number of wavelengths in the domain κL, and the size of a cell relatively to a wavelength κh.
Finally, the dependence of the estimate (ii) on κL highlights two asymptotic behaviours in $\sqrt{\kappa L}$ and $(\kappa L)^{3/2}$, according to the value of A_k, and then the flux correction polynomial functions (see Subsection 5.5).

4.2. **Proof of the well-posedness result and error estimates**

In what follows, we will detail the proof of Theorem 4.6. It will mainly rely on the introduction of one-way variables, for which the associated approximations and errors verify local strong equations. Then, error estimates will be derived going from one cell to its neighbour, and propagating the error along it in an iterative process: summing up on all the cells will thus allow to conclude.

4.2.1. *Strong equations for the one-way variables*

The interest of the Flux Reconstruction approach is that strong equations can be derived on each interval for the approximation of the solution, and then for the local error.
First, in every cell I_n, we define local flux correction polynomial functions $P_n^{\rightarrow}$ and $P_n^{\leftarrow}$ thanks to the reference flux correction polynomial functions $P^{\rightarrow}$ and $P^{\leftarrow}$ (see Definition 2.13) as

$$\forall\, x \in \mathsf{I}_n, \quad P_n^{\rightarrow}(x) = P^{\rightarrow}(\widehat{x}) \quad \text{and} \quad P_n^{\leftarrow}(x) = P^{\leftarrow}(\widehat{x}) \quad \text{with} \quad x = X_{n-1} + h\widehat{x}. \tag{78}$$

Then, to drastically simplify the continuous and discrete systems, we decompose the solution in the one-way variables

$$y^{\rightarrow} = u - v \quad \text{and} \quad y^{\leftarrow} = u + v, \tag{79}$$

with their discrete counterparts

$$y_h^{\rightarrow} = u_h - v_h \quad \text{and} \quad y_h^{\leftarrow} = u_h + v_h. \tag{80}$$

Remark 4.8. In agreement with the BCs (71), we introduce the virtual values out of the boundaries

$$y_{h,0}^{\rightarrow}(X_0) = g_1 \quad \text{and} \quad y_{h,N+1}^{\leftarrow}(X_N) = g_2. \tag{81}$$

Then, these changes of variables allow to decouple the systems of Problems 1.1 and 4.4.

Proposition 4.9 (One-way reformulation)**.** *$y^{\rightarrow}$ and $y^{\leftarrow}$ are solutions of*

$$\forall\, x \in \Omega,\ \left\{ \begin{array}{rcl} \left(y^{\rightarrow}\right)^{(1)}(x) & = & -i\kappa y^{\rightarrow}(x) \\ y^{\rightarrow}(X_0) & = & g_1 \end{array} \right. \quad \textit{and} \quad \left\{ \begin{array}{rcl} \left(y^{\leftarrow}\right)^{(1)}(x) & = & i\kappa y^{\leftarrow}(x), \\ y^{\leftarrow}(X_N) & = & g_2, \end{array} \right. \tag{82}$$

while $y_h^{\rightarrow}$ and $y_h^{\leftarrow}$ are solutions of

$$\forall\, n \in [\![1,N]\!],\ \forall\, x \in \mathsf{I}_n,\ \left\{ \begin{array}{rcl} \left(y_{h,n}^{\rightarrow}\right)^{(1)}(x) & = & -i\kappa y_{h,n}^{\rightarrow}(x) + [\![y_h^{\rightarrow}]\!]_{n-1} \left(P_n^{\rightarrow}\right)^{(1)}(x), \\ \left(y_{h,n}^{\leftarrow}\right)^{(1)}(x) & = & i\kappa y_{h,n}^{\leftarrow}(x) - [\![y_h^{\leftarrow}]\!]_{n} \left(P_n^{\leftarrow}\right)^{(1)}(x), \end{array} \right. \tag{83}$$

where we recall the jump of $w \in \mathrm{H}^1(\mathcal{T}_h)$ at any interface is denoted as

$$\forall\, n \in [\![0,N]\!],\ [\![w]\!]_n = w_{n+1}(X_n) - w_n(X_n). \tag{84}$$

Proof. Equation (82) is derived from (1) with $Z_1 = Z_2 = 1$ and the definition (79) of $y^{\rightarrow}$ and $y^{\leftarrow}$.
Equation (83) is due to the strong equation (70) verified by $\mathbf{y}_h$, the definition (80) of $y_h^{\rightarrow}$ and $y_h^{\leftarrow}$, and the following expressions of the interface corrections (which rely on the flux numerical trace operators defined thanks to (55) and (58)):

- For an internal interface $n^F \in [\![1, N-1]\!]$, one obtains

$$\gamma_{n^F}\widetilde{\boldsymbol{\phi}}_h - \boldsymbol{\phi}_{h,n^F+1}(X_{n^F}) = \frac{1}{2}\begin{pmatrix} -[\![u_h - v_h]\!]_{n^F} \\ [\![u_h - v_h]\!]_{n^F} \end{pmatrix} \quad \text{and} \quad \gamma_{n^F}\widetilde{\boldsymbol{\phi}}_h - \boldsymbol{\phi}_{h,n^F}(X_{n^F}) = -\frac{1}{2}\begin{pmatrix} [\![u_h + v_h]\!]_{n^F} \\ [\![u_h + v_h]\!]_{n^F} \end{pmatrix}. \tag{85}$$

- For the boundary interfaces, one obtains by referring to Remark 4.8

$$\gamma_0\widetilde{\boldsymbol{\phi}}_h - \boldsymbol{\phi}_{h,1}(X_0) = \frac{1}{2}\begin{pmatrix} -[\![u_h - v_h]\!]_0 \\ [\![u_h - v_h]\!]_0 \end{pmatrix} \quad \text{and} \quad \gamma_N\widetilde{\boldsymbol{\phi}}_h - \boldsymbol{\phi}_{h,N}(X_N) = -\frac{1}{2}\begin{pmatrix} [\![u_h + v_h]\!]_N \\ [\![u_h + v_h]\!]_N \end{pmatrix}, \tag{86}$$

  which can be seen as the direct application of (85) with fictive cells associated to the BCs.

□

Remark 4.10. We highlight the fact that the exact solutions of (82) can be easily obtained as

$$\forall\, x \in \Omega,\ y^{\rightarrow}(x) = g_1 e^{-i\kappa(x - X_0)} \quad \text{and} \quad y^{\leftarrow}(x) = g_2 e^{i\kappa(x - X_N)}, \tag{87}$$

which ensures that $\mathbf{y} \in \left[\mathrm{C}^{\infty}(\Omega)\right]^2$.

Proposition 4.11 (Strong error equations in one-way variables)**.** *The one-way errors*

$$\varepsilon_h^{\rightarrow} = y^{\rightarrow} - y_h^{\rightarrow} \quad \textit{and} \quad \varepsilon_h^{\leftarrow} = y^{\leftarrow} - y_h^{\leftarrow}, \tag{88}$$

satisfy the strong local equations

$$\forall\, n \in [\![1,N]\!],\ \forall\, x \in \mathsf{I}_n,\ \left\{ \begin{array}{rcl} \left(\varepsilon_{h,n}^{\rightarrow}\right)^{(1)}(x) & = & -i\kappa\varepsilon_{h,n}^{\rightarrow}(x) + [\![\varepsilon_h^{\rightarrow}]\!]_{n-1} \left(P_n^{\rightarrow}\right)^{(1)}(x), \\ \left(\varepsilon_{h,n}^{\leftarrow}\right)^{(1)}(x) & = & i\kappa\varepsilon_{h,n}^{\leftarrow}(x) - [\![\varepsilon_h^{\leftarrow}]\!]_{n} \left(P_n^{\leftarrow}\right)^{(1)}(x), \end{array} \right. \tag{89}$$

and the boundary conditions

$$\varepsilon_{h,0}^{\rightarrow}(X_0) = 0 \quad \textit{and} \quad \varepsilon_{h,N+1}^{\leftarrow}(X_N) = 0. \tag{90}$$

Proof. Equation (89) is due to (82), (83) and the continuity of $y^{\rightarrow}$ and $y^{\leftarrow}$, while (90) relies on (81) and (87). □

4.2.2. *Well-posedness of the one-way discrete problem and local error estimates*

In this Subsection, we will focus on the propagating errors, to derive preliminary local estimates. The proofs will only be detailed for $\varepsilon_h^{\rightarrow}$, as similar steps can be followed for $\varepsilon_h^{\leftarrow}$.

We begin with the proof that $y_h^{\rightarrow}$ and $y_h^{\leftarrow}$ are well defined on each interval if Conjecture 4.1 is verified, and we detail a bound on the error jump realised on $\varepsilon_h^{\rightarrow}$ and $\varepsilon_h^{\leftarrow}$ at the interface between two cells.

Proposition 4.12. *In the framework of Conjecture* 4.1*, the one-way variables $y_h^{\rightarrow}$ and $y_h^{\leftarrow}$ are well-defined in $\mathcal{V}_{h,k}$ and the error jumps are bounded as*

$$\begin{aligned} \forall\, n \in [\![0, N-1]\!], \quad |[\![\varepsilon_h^{\rightarrow}]\!]_n| &\leqslant \alpha_{\kappa h,k}^{\rightarrow} \frac{(\kappa h)^{k+1}}{|T_{k+1}^{\rightarrow}|} \left(\left|\varepsilon_{h,n}^{\rightarrow}(X_n)\right| + |g_1| \right), \\ \forall\, n \in [\![1, N]\!], \quad |[\![\varepsilon_h^{\leftarrow}]\!]_n| &\leqslant \alpha_{\kappa h,k}^{\leftarrow} \frac{(\kappa h)^{k+1}}{|T_{k+1}^{\leftarrow}|} \left(\left|\varepsilon_{h,n+1}^{\leftarrow}(X_n)\right| + |g_2| \right), \end{aligned} \tag{91}$$

where we denote the derivatives at 0 *and* 1 *of the reference flux correction polynomial functions as*

$$\forall\, l \in [\![0, k+1]\!], \quad T_l^{\rightarrow} = (P^{\rightarrow})^{(l)}(0) \quad \text{and} \quad T_l^{\leftarrow} = (P^{\leftarrow})^{(l)}(1), \tag{92}$$

and

$$\alpha_{\kappa h,k}^{\rightarrow} = \frac{(\kappa h)^{-(k+1)}\, |T_{k+1}^{\rightarrow}|}{\left| \sum_{l=0}^{k+1} (-i\kappa h)^{-l}\, T_l^{\rightarrow} \right|} \quad \text{and} \quad \alpha_{\kappa h,k}^{\leftarrow} = \frac{(\kappa h)^{-(k+1)}\, |T_{k+1}^{\leftarrow}|}{\left| \sum_{l=0}^{k+1} (i\kappa h)^{-l}\, T_l^{\leftarrow} \right|}, \tag{93}$$

with the asymptotic behaviour

$$\alpha_{\kappa h,k}^{\rightarrow} \underset{\kappa h \to 0^+}{\longrightarrow} 1 \quad \text{and} \quad \alpha_{\kappa h,k}^{\leftarrow} \underset{\kappa h \to 0^+}{\longrightarrow} 1. \tag{94}$$

Proof. First, let's consider an interval $n \in [\![1, N]\!]$ for which we suppose $y_{h,n-1}^{\rightarrow}(X_{n-1})$ is well-defined (which is the case for $n = 1$, as $y_{h,0}^{\rightarrow}(X_0) = g_1$).
By differentiating (83) $l-1$ times, we obtain for $l \in [\![1, k+1]\!]$

$$\left(y_{h,n}^{\rightarrow}\right)^{(l)}(X_{n-1}) = -i\kappa \left(y_{h,n}^{\rightarrow}\right)^{(l-1)}(X_{n-1}) + \left(y_{h,n}^{\rightarrow}(X_{n-1}) - y_{h,n-1}^{\rightarrow}(X_{n-1})\right) (P_n^{\rightarrow})^{(l)}(X_{n-1}), \tag{95}$$

and by induction

$$\left(y_{h,n}^{\rightarrow}\right)^{(l)}(X_{n-1}) = (-i\kappa)^l\, y_{h,n}^{\rightarrow}(X_{n-1}) + \left(y_{h,n}^{\rightarrow}(X_{n-1}) - y_{h,n-1}^{\rightarrow}(X_{n-1})\right) \sum_{m=1}^{l} (-i\kappa)^{l-m} (P_n^{\rightarrow})^{(m)}(X_{n-1}). \tag{96}$$

Thus, the last thing we need to characterise the polynomial function $y_{h,n}^{\rightarrow}$ (of degree at most k) is the expression of $y_{h,n}^{\rightarrow}(X_{n-1})$, as the derivatives $\left(\left(y_{h,n}^{\rightarrow}\right)^{(l)}(X_{n-1}) \right)_{l \in [\![1,k]\!]}$ can be deduced from (96). To do so, by taking $l = k+1$ in this equation and as $\left(y_{h,n}^{\rightarrow}\right)^{(k+1)}(X_{n-1}) = 0$, we get

$$(-i\kappa)^{k+1} y_{h,n}^{\rightarrow}(X_{n-1}) + \left(y_{h,n}^{\rightarrow}(X_{n-1}) - y_{h,n-1}^{\rightarrow}(X_{n-1})\right) \sum_{m=1}^{k+1} (-i\kappa)^{k+1-m} (P_n^{\rightarrow})^{(m)}(X_{n-1}) = 0. \tag{97}$$

The definition (78) of transported flux correction polynomial functions leads to

$$\forall\, m \in [\![0, k+1]\!],\ \forall\, x \in \mathsf{I}_n,\ (P_n^{\rightarrow})^{(m)}(x) = h^{-m} (P^{\rightarrow})^{(m)}(\widehat{x}) \quad \text{with} \quad x = X_{n-1} + h\widehat{x}, \tag{98}$$

and by using the fact that $T_0^{\rightarrow} = P^{\rightarrow}(0) = 1$, (97) can be rewritten as

$$\left[\sum_{l=0}^{k+1}(-i\kappa h)^{-l}\ T_l^{\rightarrow}\right] y_{h,n}^{\rightarrow}(X_{n-1}) = \left[\sum_{l=1}^{k+1}(-i\kappa h)^{-l}\ T_l^{\rightarrow}\right] y_{h,n-1}^{\rightarrow}(X_{n-1}), \tag{99}$$

where we recall that $T_l^{\rightarrow} = (P^{\rightarrow})^{(l)}(0)$, for $l \in [\![0, k+1]\!]$. Conjecture 4.1 ensures that $\sum_{l=0}^{k+1}(-i\kappa h)^{-l}\ T_l^{\rightarrow} \neq 0$: $y_{h,n}^{\rightarrow}(X_{n-1})$, and then all the derivatives $\left(\left(y_{h,n}^{\rightarrow}\right)^{(l)}(X_{n-1})\right)_{l\in[\![0,k]\!]}$, are well-defined with respect to $y_{h,n-1}^{\rightarrow}(X_{n-1})$. The local solution approximation $y_{h,n}^{\rightarrow}$ being a polynomial function of degree at most k, it is then perfectly determined. Global well-posedness is deduced by induction.
Concerning the jump estimates, we can write

$$-[\![y_h^{\rightarrow}]\!]_{n-1} = \frac{y_{h,n-1}^{\rightarrow}(X_{n-1})}{\sum_{l=0}^{k+1}(-i\kappa h)^{-l}\ T_l^{\rightarrow}}. \tag{100}$$

Artificially introducing $y^{\rightarrow}(X_{n-1}) = g_1 e^{-i\kappa X_{n-1}}$ (see (87)) to make $\varepsilon_{h,n-1}^{\rightarrow}(X_{n-1}) = (y^{\rightarrow} - y_{h,n-1}^{\rightarrow})(X_{n-1})$ appear, we get

$$[\![\varepsilon_h^{\rightarrow}]\!]_{n-1} = -[\![y_h^{\rightarrow}]\!]_{n-1} = \frac{y^{\rightarrow}(X_{n-1}) - \varepsilon_{h,n-1}^{\rightarrow}(X_{n-1})}{\sum_{l=0}^{k+1}(-i\kappa h)^{-l}\ T_l^{\rightarrow}}, \tag{101}$$

where we have used the continuity of $y^{\rightarrow}$ at $x = X_{n-1}$.
Then, the triangular inequality and the definition (93) of $\alpha_{\kappa h,k}^{\rightarrow}$ lead to

$$|[\![\varepsilon_h^{\rightarrow}]\!]_{n-1}| \leqslant \alpha_{\kappa h,k}^{\rightarrow}\frac{(\kappa h)^{k+1}}{|T_{k+1}^{\rightarrow}|}\left(|g_1| + |\varepsilon_{h,n-1}^{\rightarrow}(X_{n-1})|\right). \tag{102}$$

Finally, the asymptotic behaviour of $\alpha_{\kappa h,k}^{\rightarrow}$ results from $T_{k+1}^{\rightarrow} \neq 0$, as $P^{\rightarrow}$ is of degree $k+1$ (see Claim 4.3). □

Proposition 4.12 is the key argument to propagate the error estimate between two consecutive cells.
The next Proposition estimates $|\varepsilon_{h,n}^{\rightarrow}(X_n)|$ and $|\varepsilon_{h,n+1}^{\leftarrow}(X_n)|$, respectively at the right and left sides of each cell (see Figure 4).

Proposition 4.13. *In the framework of Conjecture* 4.1*, the propagation of the error on each interval leads to*

$$\forall\ n \in [\![0, N]\!], \quad |\varepsilon_{h,n}^{\rightarrow}(X_n)| \leqslant \left[\left(1+\gamma_{\kappa h,k}^{\rightarrow}\right)^n - 1\right]|g_1| \quad \textit{and} \quad |\varepsilon_{h,n+1}^{\leftarrow}(X_n)| \leqslant \left[\left(1+\gamma_{\kappa h,k}^{\leftarrow}\right)^{N-n} - 1\right]|g_2|, \tag{103}$$

where we denote, thanks to the definition (93) *of* $\alpha_{\kappa h,k}^{\rightarrow}$ *and* $\alpha_{\kappa h,k}^{\leftarrow}$

$$\gamma_{\kappa h,k}^{\rightarrow} = \alpha_{\kappa h,k}^{\rightarrow}\frac{|J_{\kappa h}^{\rightarrow}|}{|T_{k+1}^{\rightarrow}|}(\kappa h)^{k+1} \quad \textit{and} \quad \gamma_{\kappa h,k}^{\leftarrow} = \alpha_{\kappa h,k}^{\leftarrow}\frac{|J_{\kappa h}^{\leftarrow}|}{|T_{k+1}^{\leftarrow}|}(\kappa h)^{k+1}, \tag{104}$$

$$J_{\kappa h}^{\rightarrow} = 1 + \int_0^1 (P^{\rightarrow})^{(1)}(\widehat{x})\ e^{i\kappa h\widehat{x}}\,\mathrm{d}\widehat{x} \quad \textit{and} \quad J_{\kappa h}^{\leftarrow} = 1 - \int_0^1 (P^{\leftarrow})^{(1)}(1-\widehat{x})\ e^{i\kappa h\widehat{x}}\,\mathrm{d}\widehat{x}. \tag{105}$$

with the asymptotic behaviour

$$\gamma_{\kappa h,k}^{\rightarrow} \underset{\kappa h\to 0^+}{=} O\left((\kappa h)^{k+2}\right) \quad \textit{and} \quad \gamma_{\kappa h,k}^{\leftarrow} \underset{\kappa h\to 0^+}{=} O\left((\kappa h)^{k+2}\right). \tag{106}$$

Proof. By considering a variation of parameters on the differential equation (89) solved by $\varepsilon_h^{\rightarrow}$, we get

$$\forall\, n \in [\![1, N]\!],\ \varepsilon_{h,n}^{\rightarrow}(X_n) = \left[[\![\varepsilon_h^{\rightarrow}]\!]_{n-1} J_{\kappa h}^{\rightarrow} + \varepsilon_{h,n-1}^{\rightarrow}(X_{n-1})\right] e^{-i\kappa h}, \tag{107}$$

where we have denoted, and simplified thanks to the change of variable $x = h\widehat{x} + X_{n-1}$ and (98)

$$J_{\kappa h}^{\rightarrow} = 1 + \int_{\mathsf{I}_n} (P_n^{\rightarrow})^{(1)}(x)\, e^{i\kappa(x - X_{n-1})}\, \mathrm{d}x = 1 + \int_0^1 (P^{\rightarrow})^{(1)}(\widehat{x})\ e^{i\kappa h\widehat{x}}\, \mathrm{d}\widehat{x}. \tag{108}$$

Thus, triangular inequality and Proposition 4.12 lead to

$$|\varepsilon_{h,n}^{\rightarrow}(X_n)| \leqslant (1 + \gamma_{\kappa h,k}^{\rightarrow})|\varepsilon_{h,n-1}^{\rightarrow}(X_{n-1})| + \gamma_{\kappa h,k}^{\rightarrow}|g_1|, \tag{109}$$

where we have used the definition (104) of $\gamma_{\kappa h,k}^{\rightarrow}$.
Thus, by considerations on an arithmetico-geometric sequence, we obtain

$$\forall\, n \in [\![0, N-1]\!],\ \left(|\varepsilon_{h,n}^{\rightarrow}(X_n)| + |g_1|\right) \leqslant (1 + \gamma_{\kappa h,k}^{\rightarrow})^n\ \left(|\varepsilon_{h,0}^{\rightarrow}(X_0)| + |g_1|\right), \tag{110}$$

and (90) allows to conclude.
Finally, the asymptotic behaviour of $\gamma_{\kappa h,k}^{\rightarrow}$ comes out of Remark 4.14 and Lemma 4.15. □

Remark 4.14. We highlight two specific behaviours of $\gamma_{\kappa h,k}^{\rightarrow}$ and $\gamma_{\kappa h,k}^{\leftarrow}$ with respect to

$$A_k^{\rightarrow} = \int_0^1 P^{\rightarrow}(\widehat{x})\ \mathrm{d}\widehat{x} \quad \text{and} \quad A_k^{\leftarrow} = \int_0^1 P^{\leftarrow}(\widehat{x})\ \mathrm{d}\widehat{x}. \tag{111}$$

Indeed, by using Lemma 4.15, one has:

- If $A_k^{\rightarrow} \neq 0$ and $A_k^{\leftarrow} \neq 0$, then $\gamma_{\kappa h,k}^{\rightarrow}$ and $\gamma_{\kappa h,k}^{\leftarrow}$ can be rewritten as

$$\gamma_{\kappa h,k}^{\rightarrow} = \alpha_{\kappa h,k}^{\rightarrow}\beta_{\kappa h,k}^{\rightarrow}\frac{|A_k^{\rightarrow}|}{|T_{k+1}^{\rightarrow}|}(\kappa h)^{k+2} \quad \text{and} \quad \gamma_{\kappa h,k}^{\leftarrow} = \alpha_{\kappa h,k}^{\leftarrow}\beta_{\kappa h,k}^{\leftarrow}\frac{|A_k^{\leftarrow}|}{|T_{k+1}^{\leftarrow}|}(\kappa h)^{k+2}, \tag{112}$$

  where we denote

$$\beta_{\kappa h,k}^{\rightarrow} = \frac{|J_{\kappa h}^{\rightarrow}|}{|A_k^{\rightarrow}|\kappa h} \quad \text{and} \quad \beta_{\kappa h,k}^{\leftarrow} = \frac{|J_{\kappa h}^{\leftarrow}|}{|A_k^{\leftarrow}|\kappa h}, \tag{113}$$

  with the asymptotic behaviour

$$\beta_{\kappa h,k}^{\rightarrow} \underset{\kappa h \to 0^+}{\longrightarrow} 1 \quad \text{and} \quad \beta_{\kappa h,k}^{\leftarrow} \underset{\kappa h \to 0^+}{\longrightarrow} 1. \tag{114}$$

- Otherwise, by using the asymptotic behaviour (94) of $\alpha_{\kappa h,k}^{\rightarrow}$ and $\alpha_{\kappa h,k}^{\leftarrow}$, one has

$$\gamma_{\kappa h,k}^{\rightarrow} \underset{\kappa h \to 0^+}{=} O\left((\kappa h)^{k+3}\right) \quad \text{and} \quad \gamma_{\kappa h,k}^{\leftarrow} \underset{\kappa h \to 0^+}{=} O\left((\kappa h)^{k+3}\right). \tag{115}$$

Lemma 4.15. *We have the asymptotic estimates*

$$J_{\kappa h}^{\rightarrow} \underset{\kappa h \to 0^+}{=} -iA_k^{\rightarrow}\kappa h + O\left((\kappa h)^2\right) \quad \textit{and} \quad J_{\kappa h}^{\leftarrow} \underset{\kappa h \to 0^+}{=} -iA_k^{\leftarrow}\kappa h + O\left((\kappa h)^2\right). \tag{116}$$

Proof. Let's first note that

$$\int_0^1 (P^{\rightarrow})^{(1)}(\widehat{x})\ \mathrm{d}\widehat{x} = P^{\rightarrow}(1) - P^{\rightarrow}(0) = -1, \tag{117}$$

which allows to rewrite $J_{\kappa h}^{\rightarrow}$ as

$$J_{\kappa h}^{\rightarrow} = \int_0^1 \left(P^{\rightarrow}\right)^{(1)}(\hat{x}) \left(e^{i\kappa h \hat{x}} - 1\right) \mathrm{d}\hat{x}. \tag{118}$$

By writing $e^{i\kappa h\hat{x}} - 1 \underset{\kappa h \to 0^+}{=} i\kappa h\hat{x} + O\left((\kappa h)^2\right)$ for $\hat{x} \in [0,1]$, an integration by parts leads to

$$J_{\kappa h}^{\rightarrow} \underset{\kappa h \to 0^+}{=} i\kappa h \left[-\int_0^1 P^{\rightarrow}(\hat{x}) \, \mathrm{d}\hat{x} + \left[\hat{x}\, P^{\rightarrow}(\hat{x})\right]_0^1 \right] + \int_0^1 \left(P^{\rightarrow}\right)^{(1)}(\hat{x}) \, O\left((\kappa h)^2\right) \mathrm{d}\hat{x}. \tag{119}$$

According to the fact that $P^{\rightarrow}(1) = 0$ and the definition (111) of $A_k^{\rightarrow}$, we get

$$i\kappa h \left[-\int_0^1 P^{\rightarrow}(\hat{x}) \, \mathrm{d}\hat{x} + \left[\hat{x}\, P^{\rightarrow}(\hat{x})\right]_0^1 \right] = -i\kappa h A_k^{\rightarrow}. \tag{120}$$

Finally, a Cauchy-Schwarz inequality ensures that, for κh small enough

$$\int_0^1 \left(P^{\rightarrow}\right)^{(1)}(\hat{x}) \, O\left((\kappa h)^2\right) \mathrm{d}\hat{x} \lesssim (\kappa h)^2 \left\| \left(P^{\rightarrow}\right)^{(1)} \right\|_{\mathrm{L}^2(0,1)}. \tag{121}$$

□

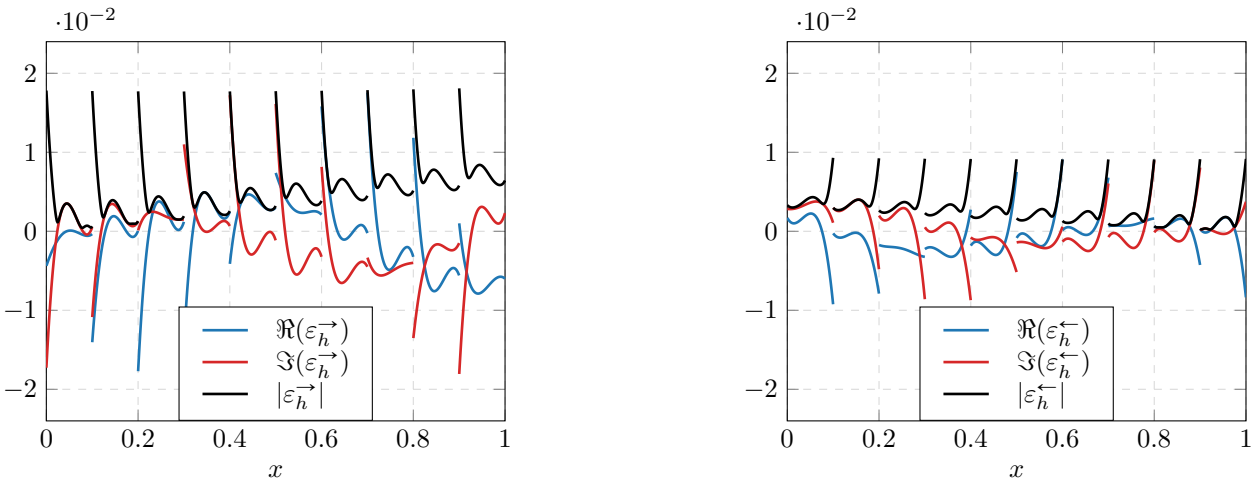

(I) $\varepsilon_h^{\rightarrow}$ (II) $\varepsilon_h^{\leftarrow}$

FIGURE 4. Visualisation of $\varepsilon_h^{\rightarrow}$ and $\varepsilon_h^{\leftarrow}$ along Ω for $L = 1$, $N = 10$, the parameters of Table 1 and configuration SD_CLo (see Section 5): error 'absorption' in each cell and global accumulation with propagation towards right and left respectively.

4.2.3. *Global error estimates in the one-way framework*

Note 4.16. For the rest of this Section, we recall that the notation $A \lesssim B$ means that there exists a constant $C > 0$, independent of κ, h, k and L, such that we have $A \leqslant B\, C$.
Moreover, the following estimates will be derived in an asymptotic regime, for κh small enough, which ensures that Conjecture 4.1 is verified (see Remark 4.2): all the local estimates of Subsection 4.2.2 are then valid.

This finally leads to a bound on the jump at each interface, and then on the weak semi-norm $|\cdot|_{\square}$.

Proposition 4.17. *The jump error at any internal interface is bounded, for κh small enough, by*

$$\forall\, n \in [\![0, N-1]\!], \quad |[\![\varepsilon_h^{\rightarrow}]\!]_n| \lesssim \frac{(\kappa h)^{k+1}}{|T_{k+1}^{\rightarrow}|}|g_1| \quad \textit{and} \quad |[\![\varepsilon_h^{\leftarrow}]\!]_{n+1}| \lesssim \frac{(\kappa h)^{k+1}}{|T_{k+1}^{\leftarrow}|}|g_2|, \tag{122}$$

which ensures the following bounds of the semi-norm of propagating errors

$$|\varepsilon_h^{\rightarrow}|_{\square}^2 \lesssim (\kappa L)\frac{(\kappa h)^{2k+1}}{|T_{k+1}^{\rightarrow}|^2}\,|g_1|^2 \quad \textit{and} \quad |\varepsilon_h^{\leftarrow}|_{\square}^2 \lesssim (\kappa L)\frac{(\kappa h)^{2k+1}}{|T_{k+1}^{\leftarrow}|^2}\,|g_2|^2. \tag{123}$$

Proof. First, by merging Propositions 4.12 and 4.13, we directly get

$$\forall\, n \in [\![1, N-1]\!],\ |[\![\varepsilon_h^{\rightarrow}]\!]_n| \leqslant \alpha_{\kappa h,k}^{\rightarrow}\frac{(\kappa h)^{k+1}}{|T_{k+1}^{\rightarrow}|}(1+\gamma_{\kappa h,k}^{\rightarrow})^n|g_1|. \tag{124}$$

Yet, as $N = Lh^{-1}$ and by using the asymptotic behaviour (106) of $\gamma_{\kappa h,k}^{\rightarrow}$, one has for any $n \in [\![1, N-1]\!]$

$$\left(1+\gamma_{\kappa h,k}^{\rightarrow}\right)^n \underset{\kappa h\to 0^+}{=} 1 + O\left((\kappa L)(\kappa h)^{k+1}\right), \tag{125}$$

which justifies the bound of (122) for κh small enough, with the asymptotic behaviour (94) of $\alpha_{\kappa h,k}^{\rightarrow}$. Moreover, recalling that $N = Lh^{-1}$, we have

$$\sum_{n=0}^{N-1}\left(1+\gamma_{\kappa h,k}^{\rightarrow}\right)^{2n} \underset{\kappa h\to 0^+}{=} \frac{\kappa L}{\kappa h} + O\left((\kappa L)^2(\kappa h)^k\right), \tag{126}$$

which implies, for κh small enough, that

$$\sum_{n=0}^{N-1}|[\![\varepsilon_h^{\rightarrow}]\!]_n|^2 \underset{\kappa h\to 0^+}{=} \left[\frac{\kappa L}{\kappa h} + O\left((\kappa L)^2(\kappa h)^k\right)\right]\left[\alpha_{\kappa h,k}^{\rightarrow}\frac{(\kappa h)^{k+1}}{|T_{k+1}^{\rightarrow}|}|g_1|\right]^2. \tag{127}$$

For the boundary terms, we have thanks to (90)

$$|\varepsilon_{h,1}^{\rightarrow}(X_0)|^2 = |[\![\varepsilon_h^{\rightarrow}]\!]_0|^2, \tag{128}$$

and according to Proposition 4.13

$$|\varepsilon_{h,N}^{\rightarrow}(X_N)|^2 \underset{\kappa h\to 0^+}{=} \left[O\left((\kappa L)(\kappa h)^{k+1}\right)|g_1|\right]^2. \tag{129}$$

Finally, by recalling the definition (72) of $|\varepsilon_h^{\rightarrow}|_{\square}$, the right boundary term can be neglected for κh small enough: this gives the expected semi-norm bounding as $\alpha_{\kappa h,k}^{\rightarrow}$ has limit 1 as κh tends to 0^+. □

Then, let's consider the L^2 norm of the error.

Proposition 4.18. *We have the following bound of the L^2 norm of the error for κh small enough*

$$\|\varepsilon_h^{\rightarrow}\|_0^2 \lesssim L\frac{|B_k^{\rightarrow}|^2 + \frac{1}{3}(\kappa L)^2|A_k^{\rightarrow}|^2}{|T_{k+1}^{\rightarrow}|^2}(\kappa h)^{2k+2}|g_1|^2 \quad \textit{and} \quad \|\varepsilon_h^{\leftarrow}\|_0^2 \lesssim L\frac{|B_k^{\leftarrow}|^2 + \frac{1}{3}(\kappa L)^2|A_k^{\leftarrow}|^2}{|T_{k+1}^{\leftarrow}|^2}(\kappa h)^{2k+2}|g_2|^2, \tag{130}$$

where we denote

$$B_k^{\rightarrow} = \|P^{\rightarrow}\|_{\mathrm{L}^2(0,1)} \quad \textit{and} \quad B_k^{\leftarrow} = \|P^{\leftarrow}\|_{\mathrm{L}^2(0,1)}. \tag{131}$$

Proof. Let's take back the expression of $\varepsilon_h^{\rightarrow}$ obtained by variation of parameters: for any $n \in [\![1, N]\!]$, we have

$$\forall\, x \in \mathsf{I}_n,\ \varepsilon_{h,n}^{\rightarrow}(x) = \left[[\![\varepsilon_h^{\rightarrow}]\!]_{n-1} \left(1 + \int_{X_{n-1}}^{x} (P_n^{\rightarrow})^{(1)}(t)\, e^{i\kappa(t-X_{n-1})}\, \mathrm{d}t \right) + \varepsilon_{h,n-1}^{\rightarrow}(X_{n-1}) \right] e^{-i\kappa(x-X_{n-1})}. \quad (132)$$

Thus, by triangular and Young's inequalities, one has

$$\forall\, n \in [\![1, N]\!],\ \|\varepsilon_{h,n}^{\rightarrow}\|^2_{\mathrm{L}^2(\mathsf{I}_n)} \lesssim K_n^{\rightarrow}(h)\, |[\![\varepsilon_h^{\rightarrow}]\!]_{n-1}|^2 + h\, |\varepsilon_{h,n-1}^{\rightarrow}(X_{n-1})|^2, \quad (133)$$

where we have denoted

$$K^{\rightarrow}(h) = \int_{\mathsf{I}_n} \left| 1 + \int_{X_{n-1}}^{x} (P_n^{\rightarrow})^{(1)}(t)\, e^{i\kappa(t-X_{n-1})}\, \mathrm{d}t \right|^2 \mathrm{d}x. \quad (134)$$

Then, by using Propositions 4.13 and 4.17 and Lemma 4.19, we obtain for κh small enough

$$\forall\, n \in [\![1, N]\!],\ \|\varepsilon_h^{\rightarrow}\|^2_{\mathrm{L}^2(\mathsf{I}_n)} \lesssim h \left[\frac{|B_k^{\rightarrow}|^2}{|T_{k+1}^{\rightarrow}|^2} (\kappa h)^{2k+2} + \left((1 + \gamma_{\kappa h,k}^{\rightarrow})^{n-1} - 1 \right)^2 \right] |g_1|^2. \quad (135)$$

Thus, by summing over n from 1 to $N = Lh^{-1}$, we obtain

$$\|\varepsilon_{h,n}^{\rightarrow}\|_0^2 \lesssim \left[L \frac{|B_k^{\rightarrow}|^2}{|T_{k+1}^{\rightarrow}|^2} (\kappa h)^{2k+2} + h S_{\kappa h,k}^{\rightarrow} \right] |g_1|^2, \quad (136)$$

where we have denoted

$$S_{\kappa h,k}^{\rightarrow} = \sum_{n=1}^{N} \left[(1 + \gamma_{\kappa h,k}^{\rightarrow})^{n-1} - 1 \right]^2. \quad (137)$$

Finally, reporting Lemma 4.20 in this bounding gives the expected estimate for κh small enough:

- If $A_k^{\rightarrow} \neq 0$, we obtain the expected estimate.
- Otherwise, $h S_{\kappa h,k}^{\rightarrow}$ can be absorbed by the other term, and the estimate is still valid (with $A_k^{\rightarrow} = 0$).

□

Lemma 4.19. *For any $n \in [\![1, N]\!]$, we have the bound*

$$K_n^{\rightarrow}(h) = \int_{\mathsf{I}_n} \left| 1 + \int_{X_{n-1}}^{x} (P_n^{\rightarrow})^{(1)}(t)\, e^{i\kappa(t-X_{n-1})}\, \mathrm{d}t \right|^2 \mathrm{d}x \lesssim \delta_{\kappa h,k}^{\rightarrow} h |B_k^{\rightarrow}|^2, \quad (138)$$

where we denote

$$\delta_{\kappa h,k}^{\rightarrow} = 1 + |B_k^{\rightarrow}|^{-2} \int_0^1 \left| \int_0^{\hat{z}} (P^{\rightarrow})^{(1)}(\hat{r}) \left(e^{i\kappa h \hat{r}} - 1 \right) \mathrm{d}\hat{r} \right|^2 \mathrm{d}\hat{z}, \quad (139)$$

with the asymptotic behaviour

$$\delta_{\kappa h,k}^{\rightarrow} \underset{\kappa h \to 0^+}{\longrightarrow} 1. \quad (140)$$

Proof. First, let's observe that $K_n^{\rightarrow}(h)$ is independent of n, as the the changes of variable $x = h\hat{z} + X_{n-1}$ and $t = h\hat{r} + X_{n-1}$ and (98) ensure that

$$K_n^{\rightarrow}(h) = h \int_0^1 \left| 1 + \int_0^{\hat{z}} (P^{\rightarrow})^{(1)}(\hat{r})\, e^{i\kappa h \hat{r}}\, \mathrm{d}\hat{r} \right|^2 \mathrm{d}\hat{z} \quad (141)$$

that we denote $K^{\rightarrow}(h)$ for the rest of the proof. Then, let's note that

$$\forall\ \widehat{z} \in [0,1],\ \int_0^{\widehat{z}} (P^{\rightarrow})^{(1)}(\widehat{r})\,\mathrm{d}\widehat{r} = P^{\rightarrow}(\widehat{z}) - 1, \tag{142}$$

which allows to rewrite $K^{\rightarrow}(h)$ as

$$K^{\rightarrow}(h) = h\int_0^1 \left| P^{\rightarrow}(\widehat{z}) + \int_0^{\widehat{z}} (P^{\rightarrow})^{(1)}(\widehat{r})\ \left(e^{i\kappa h\widehat{r}} - 1\right)\ \mathrm{d}\widehat{r}\right|^2 \mathrm{d}\widehat{z}. \tag{143}$$

Thus, Young's inequality allows to separate the bounding of $K^{\rightarrow}(h)$ in two terms which will be treated separately

$$K^{\rightarrow}(h) \lesssim h\,|B_k^{\rightarrow}|^2 + h\int_0^1 \left|\int_0^{\widehat{z}} (P^{\rightarrow})^{(1)}(\widehat{r})\ \left(e^{i\kappa h\widehat{r}} - 1\right)\ \mathrm{d}\widehat{r}\right|^2 \mathrm{d}\widehat{z}. \tag{144}$$

Focusing on the second term denoted as $M^{\rightarrow}(h)$, the Cauchy-Schwarz inequality leads, for κh small enough, to

$$M^{\rightarrow}(h) = h\int_0^1 \left|\int_0^{\widehat{z}} (P^{\rightarrow})^{(1)}(\widehat{r})\ \left(e^{i\kappa h\widehat{r}} - 1\right)\ \mathrm{d}r\right|^2 \mathrm{d}\widehat{z} \lesssim \kappa^2 h^3 \left\|(P^{\rightarrow})^{(1)}\right\|^2_{\mathrm{L}^2(0,1)} \tag{145}$$

Finally, by introducing $\delta^{\rightarrow}_{\kappa h,k} = 1 + \dfrac{M^{\rightarrow}(h)}{h\,|B_k^{\rightarrow}|^2}$, this allows to conclude. □

Lemma 4.20. *Since $N = Lh^{-1}$, we have the following asymptotic estimate*

$$S^{\rightarrow}_{\kappa h,k} = \sum_{n=1}^{N} \left[(1+\gamma^{\rightarrow}_{\kappa h,k})^{n-1} - 1\right]^2 \underset{\kappa h\to 0^+}{=} \frac{(\kappa L)^3}{3}\frac{|A_k^{\rightarrow}|^2}{|T_{k+1}^{\rightarrow}|^2}(\kappa h)^{2k+1} + o\left((\kappa h)^{2k+1}\right). \tag{146}$$

Proof. We develop the expression of $S^{\rightarrow}_{\kappa h,k}$

$$S^{\rightarrow}_{\kappa h,k} = \sum_{n=0}^{N-1} \left[(1+\gamma^{\rightarrow}_{\kappa h,k})^{2n} - 2(1+\gamma^{\rightarrow}_{\kappa h,k})^{n} + 1\right] = \frac{(1+\gamma^{\rightarrow}_{h,k})^{2L/h} - 1}{2\gamma^{\rightarrow}_{h,k} + (\gamma^{\rightarrow}_{h,k})^2} - 2\frac{(1+\gamma^{\rightarrow}_{h,k})^{L/h} - 1}{\gamma^{\rightarrow}_{h,k}} + \frac{L}{h}, \tag{147}$$

and realise series expansions of the different terms using the fact that, for κh small enough, $\gamma^{\rightarrow}_{\kappa h,k} \lesssim (\kappa h)^{k+2}$. □

Finally, a similar estimate can be derived for the H^1-broken semi-norm.

Proposition 4.21. *We have the following bound of the H^1-broken semi-norm of the error for κh small enough*

$$|\varepsilon_h^{\rightarrow}|^2_{1,h} \lesssim \kappa(\kappa L)(\kappa h)^{2k}\frac{|C_k^{\rightarrow}|^2}{|T_{k+1}^{\rightarrow}|^2}|g_1|^2 \quad \textit{and} \quad |\varepsilon_h^{\leftarrow}|^2_{1,h} \lesssim \kappa(\kappa L)(\kappa h)^{2k}\frac{|C_k^{\leftarrow}|^2}{|T_{k+1}^{\leftarrow}|^2}|g_2|^2, \tag{148}$$

where we denote

$$C_k^{\rightarrow} = \left\|(P^{\rightarrow})^{(1)}\right\|_{\mathrm{L}^2(0,1)} \quad \textit{and} \quad C_k^{\leftarrow} = \left\|(P^{\leftarrow})^{(1)}\right\|_{\mathrm{L}^2(0,1)}. \tag{149}$$

Proof. Let's take back the differential equation verified by $\varepsilon_h^{\rightarrow}$ on each cell

$$\forall\ n \in [\![1,N]\!],\ \forall\ x \in \mathsf{I}_n,\ \left(\varepsilon^{\rightarrow}_{h,n}\right)^{(1)}(x) = -i\kappa\varepsilon^{\rightarrow}_{h,n}(x) + [\![\varepsilon_h^{\rightarrow}]\!]_{n-1}\,(P_n^{\rightarrow})^{(1)}(x). \tag{150}$$

Thus, we obtain by triangular and Young's inequalities

$$\forall\, n \in [\![1,N]\!],\ \left\| \left(\varepsilon^{\rightarrow}_{h,n}\right)^{(1)} \right\|^2_{\mathrm{L}^2(\mathrm{I}_n)} \lesssim \kappa^2 \|\varepsilon^{\rightarrow}_{h,n}\|^2_{\mathrm{L}^2(\mathrm{I}_n)} + |[\![\varepsilon^{\rightarrow}_h]\!]_{n-1}|^2 \left\| (P^{\rightarrow}_n)^{(1)} \right\|^2_{\mathrm{L}^2(\mathrm{I}_n)}. \tag{151}$$

Yet, (98) ensures that

$$\left\| (P^{\rightarrow}_n)^{(1)} \right\|_{\mathrm{L}^2(\mathrm{I}_n)} = \frac{1}{h^{1/2}} \left\| (P^{\rightarrow})^{(1)} \right\|_{\mathrm{L}^2(0,1)}, \tag{152}$$

and summing over n from 1 to $N = h^{-1}L$ with the jump estimate of Proposition 4.17 leads to

$$|\varepsilon^{\rightarrow}_h|^2_{1,h} \lesssim \kappa^2 \|\varepsilon^{\rightarrow}_h\|^2_0 + \kappa \frac{(\kappa L)(\kappa h)^{2k}}{|T^{\rightarrow}_{k+1}|^2} \left\| (P^{\rightarrow})^{(1)} \right\|^2_{\mathrm{L}^2(0,1)} |g_1|^2. \tag{153}$$

Finally, the L^2-broken norm estimate of Proposition 4.18 allows to neglect the first term when κh is small enough, and then to conclude. □

4.2.4. *FR formulation well-posedness and global error estimates*

Finally, we gather the precedent results to prove Theorem 4.6.

Proof. Proposition 4.12 ensures that $y^{\rightarrow}_h$ and $y^{\leftarrow}_h$ are well-defined on each interval, in the framework of Conjecture 4.1. Then, by inverting their definitions (80), we get

$$\forall\, n \in [\![1,N]\!], \quad u_{h,n} = \frac{y^{\rightarrow}_{h,n} + y^{\leftarrow}_{h,n}}{2} \quad \text{and} \quad v_{h,n} = \frac{y^{\leftarrow}_{h,n} - y^{\rightarrow}_{h,n}}{2}, \tag{154}$$

which ensures that $\mathbf{y}_h$ is also uniquely defined in $\boldsymbol{\mathcal{V}}_{h,k}$.
Concerning the error estimates, the proof is exactly the same in the three cases, and we will then only present it for (i), the semi-norm $|\cdot|_{\square}$.
By definition, we have

$$|\boldsymbol{\varepsilon}_h|^2_{\square} = |u - u_h|^2_{\square} + |v - v_h|^2_{\square}, \tag{155}$$

and by using the definition (88) of $\varepsilon^{\rightarrow}_h$ and $\varepsilon^{\leftarrow}_h$, we obtain thanks to the triangular and Young's inequalities

$$\begin{aligned} |\boldsymbol{\varepsilon}_h|^2_{\square} &\lesssim |\varepsilon^{\rightarrow}_h + \varepsilon^{\leftarrow}_h|^2_{\square} + |\varepsilon^{\leftarrow}_h - \varepsilon^{\rightarrow}_h|^2_{\square} \\ &\lesssim |\varepsilon^{\rightarrow}_h|^2_{\square} + |\varepsilon^{\leftarrow}_h|^2_{\square}. \end{aligned} \tag{156}$$

Thus, Proposition 4.17 allows to conclude.
Similarly, Proposition 4.18 is used for (ii), while Proposition 4.21 corresponds to (iii). □

5. Numerical validations for the time-harmonic 1D wave equations

After the introduction of the error estimates of Theorem 4.6, this section will aim at illustrating them through numerical experiments.

To do so, we take back Problem 4.4 in a domain $\Omega = [0, L]$, with a uniform mesh of $N \in \mathbb{N}^*$ cells of size $h = \dfrac{L}{N}$. In all the following experiments, we consider the parameters summarised in Table 1 with uniform polynomial degree k and flux correction polynomial functions in all the cells.

Concerning the flux correction polynomial functions, we will focus on 'symmetrical couples' of degree exactly $k+1$ (as proposed in [20, 44]), in that

$$\forall\, x \in [0,1],\ P^{\leftarrow}(x) = P^{\rightarrow}(1-x), \tag{157}$$

κ	g_1	g_2
2π	$2.3+0.4i$	$-1.2i$

TABLE 1. Common characteristics to the different simulation configurations.

which avoids asymmetrical behaviours for waves coming from the left and the right. Indeed, exchanging the BCs will have no effect on the solution precision and no direction will be favored. Moreover, referring to the constants of (77), this implies

$$A_k = |A_k^{\rightarrow}| = |A_k^{\leftarrow}|, \quad B_k = |B_k^{\rightarrow}| = |B_k^{\leftarrow}|, \quad C_k = |C_k^{\rightarrow}| = |C_k^{\leftarrow}| \quad \text{and} \quad T_{k+1} = |T_{k+1}^{\rightarrow}| = |T_{k+1}^{\leftarrow}|, \tag{158}$$

where A_k, B_k, C_k and T_{k+1} are referred as '**flux correction polynomial constants**'. Similarly, the 'estimate constants' of (76) will be denoted as $\mathsf{C}_{\square} = \mathsf{C}_{\square}^{\rightarrow} = \mathsf{C}_{\square}^{\leftarrow}$ and so on.
In particular, the numerical experiments will be realised for four different families, for which $P^{\rightarrow}$ is defined as:

- The first Lagrange polynomial associated to the Chebyshev-Lobatto nodes

$$\forall\, l \in [\![0, k+1]\!],\ x_l^{CLo} = \frac{1}{2}\left(1 - \cos\left(\frac{l}{k+1}\pi\right)\right) \quad \text{and} \quad \forall\, x \in [0,1],\ P^{\rightarrow}(x) = \prod_{l \in [\![1,k+1]\!]} \frac{x - x_l^{CLo}}{x_0^{CLo} - x_l^{CLo}}. \tag{159}$$

  According to Remark 2.16, the associated FR formulation can then be seen as a SD one in this configuration: it will then be referred as SD_CLo.
- The first Lagrange polynomial associated to the Internal Gauss nodes $(x_l^{IG})_{l \in [\![0,k+1]\!]}$.
  $(x_l^{IG})_{l \in [\![1,k]\!]}$ are defined as the roots of the Legendre polynomial of degree k (translated to $[0,1]$), referred as $P_k^{Legendre}$, while $x_0^{IG} = 0$ and $x_{k+1}^{IG} = 1$. This then leads to

$$\forall\, x \in [0,1],\ P^{\rightarrow}(x) = \prod_{l \in [\![1,k+1]\!]} \frac{x - x_l^{IG}}{x_0^{IG} - x_l^{IG}}. \tag{160}$$

  Similarly to the previous case, the associated FR formulation will be referred as SD_IG.
- The right Radau polynomial of degree $k+1$ defined as

$$\forall\, x \in [0,1],\ P^{\rightarrow}(x) = P_{k+1}^{Radau}(x) = \frac{(-1)^{k+1}}{2}\left(P_{k+1}^{Legendre}(x) - P_k^{Legendre}(x)\right). \tag{161}$$

  In particular, it is orthogonal to all the polynomial functions of degree at most $k-1$, denoted as $\mathbb{P}_{k-1}([0,1])$. The associated FR formulation will then be referred as FR_Radau.
  In this linear configuration, this method can also be seen as a nodal DG formulation using the same flux numerical traces [2, 20].
- The G2 polynomial (according to Huynh's original denomination in [20]) of degree $k+1$ defined as

$$\forall\, x \in [0,1],\ P^{\rightarrow}(x) = P_{k+1}^{G2}(x) = \frac{k}{2k+1} P_{k+1}^{Radau}(x) + \frac{k+1}{2k+1} P_k^{Radau}(x). \tag{162}$$

  In particular, it is orthogonal to all the polynomial functions of $\mathbb{P}_{k-2}([0,1])$ and verifies $\left(P_{k+1}^{G2}\right)^{(1)}(1) = 0$. The associated FR formulation will then be referred as FR_G2.

Remark 5.1. One will note that in the case $k = 0$, the flux correction polynomial functions must be defined as

$$\forall\, x \in [0,1],\ P^{\rightarrow}(x) = 1 - x \quad \text{and} \quad P^{\leftarrow}(x) = x, \tag{163}$$

because of (44). Then, we will only focus on the cases $k \geqslant 1$ for which the four families differ.

First, this Section will numerically verify Conjecture 4.1 for these flux correction polynomial functions of different degrees. Then, it will present the evolution of the associated estimate constants before illustrating error behaviours relatively to various parameters: a study of the h-convergence, an overview of the k-convergence and a focus on the κL-dependence.

5.1. **Numerical validation of Conjecture** 4.1

As highlighted in the proof Subsection 4.2, the well-posedness of the FR method relies on Conjecture 4.1. We will then numerically verify it for the four families of flux correction polynomial functions.

k	SD_CLo		SD_IG		FR_Radau		FR_G2	
1	$0.37 \pm 0.33i$		0.38 ± 0.33i		0.33 ± 0.24i		0.5 ± 0.5i	
2	0.15 ± 0.25i	0.36	0.17 ± 0.24i	0.33	0.16 ± 0.18i	0.27	0.18 ± 0.27i	0.38
3	0.08 ± 0.18i	0.24 ± 0.1i	0.09 ± 0.17i	0.22 ± 0.08i	0.1 ± 0.14i	0.19 ± 0.06i	0.1 ± 0.19i	0.23 ± 0.09i

TABLE 2. Numerical approximation of the roots of polynomial $T^{\rightarrow}$ for the different flux correction polynomial families and polynomial degrees $k \in [\![1, 3]\!]$.

To do so, Table 2 presents the roots of the polynomial $T^{\rightarrow}$ (defined in (69)) for the different flux correction families and various polynomial degrees k: the key point is that none of them is purely imaginary.
Indeed, according to Remark 4.2, the Conjecture is verified if and only if $(-i\kappa h)^{-1}$ and $(i\kappa h)^{-1}$ are not roots of $T^{\rightarrow}$ and $T^{\leftarrow}$ respectively. Moreover, as correction symmetry (157) implies that $T^{\leftarrow}(X) = T^{\rightarrow}(-X)$ and none of them admits a purely imaginary root, the FR method is well-posed for any mesh in these configurations.
We also insist on the fact that all the numerical experiments we intended have fallen within the framework of the Conjecture 4.1.

5.2. **Flux correction polynomial constants**

We present in Table 3 the evolution of the constants A_k, B_k, C_k and T_{k+1} according to the polynomial degree k, for the four flux correction polynomial families we introduced.

	SD_CLo				SD_IG				FR_Radau				FR_G2			
k	A_k	B_k	C_k	T_{k+1}	A_k	B_k	C_k	T_{k+1}	A_k	B_k	C_k	T_{k+1}	A_k	B_k	C_k	T_{k+1}
1	0.17	0.37	1.53	4	0.17	0.37	1.53	4	0.0	0.37	2.0	6	0.33	0.45	1.15	2
2	5.56×10^{-2}	0.27	2.19	32	0.0	0.28	2.41	36	0.0	0.29	3.0	60	0.0	0.29	2.19	24
3	3.33×10^{-2}	0.21	2.88	384	0.0	0.23	3.36	480	0.0	0.25	4.0	840	0.0	0.24	3.21	360
4	2.0×10^{-2}	0.18	3.57	6144	0.0	0.2	4.33	8400	0.0	0.22	5.0	15120	0.0	0.21	4.22	6720

TABLE 3. Evolution of the flux correction polynomial constants for the different flux correction families and polynomial degrees $k \in [\![1, 4]\!]$.

In particular, one will note the decreasing behaviours of A_k and B_k, while C_k and T_{k+1} show an opposite behaviour. Thus, the constants $\mathsf{C}_{\square}$ and $\mathsf{C}_{\mathrm{L}^2}$ will naturally decrease (and then improve their respective convergence constants) with k, while the behaviour of $\mathsf{C}_{\mathrm{H}^1}$ will depend on the considered correction.
Moreover, an important remark is that the value of A_k for SD_IG, FR_Radau and FR_G2 is 0 for $k \geqslant 2$ (due to their orthogonality properties to polynomial spaces). Coming back to the definition (76) of $\mathsf{C}_{\mathrm{L}^2}$ and Remark 4.7, one will then expect them to show a $\sqrt{\kappa L}$-dependence for their $\|\boldsymbol{\varepsilon}_h\|_0$ estimate (see Subsection 5.5).

5.3. h-convergence: mesh refinement influence

In this Subsection, we focus on the h-convergence of the method. Then, we fix the value $L = 1$ and we make the number of cells $N = Lh^{-1}$ vary: the objective is to highlight the behaviour of the method for different polynomial orders k when the mesh is refined.
For a given error norm $|\boldsymbol{\varepsilon}_h|$ (along the three ones we introduced in Definition 4.5) and a cell number $N \geqslant 2$, the estimate of the convergence rate r_N is given thanks to the error norm values for $N \pm 1$ cells, respectively denoted $|\boldsymbol{\varepsilon}_h|_{N\pm1}$, as

$$r_N = \frac{\log_{10}(|\boldsymbol{\varepsilon}_h|_{N+1}) - \log_{10}(|\boldsymbol{\varepsilon}_h|_{N-1})}{\log_{10}(N+1) - \log_{10}(N-1)}. \tag{164}$$

Then, Tables 4, 5 and 6 present the values of r_N and the relative error norms $|\boldsymbol{\varepsilon}_h|^{rel}_{\square}$, $\|\boldsymbol{\varepsilon}_h\|^{rel}_0$ and $|\boldsymbol{\varepsilon}_h|^{rel}_{1,h}$ respectively (with respect to the norm of the exact solution), when the mesh is refined.
In accordance with the estimates (75) of Theorem 4.6, quasi-optimal convergence orders are shown for the three error estimates when κh tends to 0.
Moreover, we highlight the fact that the SD_CLo and FR_G2 method have shown inferior abilities to FR_Radau in this harmonic framework, as it had already been observed for CFD problems [5, 42].

		SD_CLo		SD_IG		FR_Radau		FR_G2	
k	N	$\lvert\boldsymbol{\varepsilon}_h\rvert^{rel}_{\square}$	r_N	$\lvert\boldsymbol{\varepsilon}_h\rvert^{rel}_{\square}$	r_N	$\lvert\boldsymbol{\varepsilon}_h\rvert^{rel}_{\square}$	r_N	$\lvert\boldsymbol{\varepsilon}_h\rvert^{rel}_{\square}$	r_N
	5	0.55	-0.99	0.55	-0.99	0.37	-1.21	0.88	-0.36
1	22	6.9×10^{-2}	-1.51	6.9×10^{-2}	-1.51	4.49×10^{-2}	-1.49	0.15	-1.55
	100	7.02×10^{-3}	-1.51	7.02×10^{-3}	-1.51	4.65×10^{-3}	-1.5	1.43×10^{-2}	-1.52
	5	9.64×10^{-2}	-2.45	8.37×10^{-2}	-2.41	4.98×10^{-2}	-2.39	0.13	-2.39
2	22	2.42×10^{-3}	-2.5	2.14×10^{-3}	-2.5	1.28×10^{-3}	-2.5	3.21×10^{-3}	-2.5
	100	5.48×10^{-5}	-2.5	4.87×10^{-5}	-2.5	2.92×10^{-5}	-2.5	7.31×10^{-5}	-2.5
	5	1.0×10^{-2}	-3.44	7.95×10^{-3}	-3.43	4.54×10^{-3}	-3.43	1.06×10^{-2}	-3.43
3	22	5.74×10^{-5}	-3.5	4.59×10^{-5}	-3.5	2.62×10^{-5}	-3.5	6.12×10^{-5}	-3.5
	100	2.87×10^{-7}	-3.5	2.3×10^{-7}	-3.5	1.31×10^{-7}	-3.5	3.06×10^{-7}	-3.5
	5	7.9×10^{-4}	-4.45	5.75×10^{-4}	-4.45	3.2×10^{-4}	-4.45	7.18×10^{-4}	-4.44
4	22	1.02×10^{-6}	-4.5	7.49×10^{-7}	-4.5	4.16×10^{-7}	-4.5	9.37×10^{-7}	-4.5
	100	1.13×10^{-9}	-4.5	8.24×10^{-10}	-4.5	4.58×10^{-10}	-4.5	1.03×10^{-9}	-4.5

TABLE 4. Evolution of the relative error $|\boldsymbol{\varepsilon}_h|^{rel}_{\square}$ according to the number of mesh cells N and the polynomial degree k.

5.4. k-convergence: polynomial degree influence

Then, we focus on the k-convergence of the method. Then, we fix the values $L = 1$ and $N = 4$, and we make the polynomial degree k vary: the objective is to highlight the behaviour of the method, depending on the flux correction polynomial functions, when k increases.
Then, Figure 5 presents the relative values of the errors $|\boldsymbol{\varepsilon}_h|^{rel}_{\square}$, $\|\boldsymbol{\varepsilon}_h\|^{rel}_0$ and $|\boldsymbol{\varepsilon}_h|^{rel}_{1,h}$ respectively, when the polynomial degree evolves. One will note comparable behaviours, as the error decreases in similar ways for all the flux correction polynomial families, as it could be expected.

5.5. κL-dependence of the errors

Finally, we focus on the error dependence on κL: the objective is to highlight the behaviour of the method when the number of wavelengths in the domain becomes larger and larger.
So as to get comparable experiments in this subsection, we fix the number of degrees of freedom (dof) per wavelength, $N_{dof/\lambda} = \frac{2\pi(k+1)}{\kappa h}$, to a constant value $N_{dof/\lambda} = 600$. Then, $\kappa = 2\pi$ is let constant, while various

		SD_CLo		SD_IG		FR_Radau		FR_G2	
k	N	$\|\boldsymbol{\varepsilon}_h\|_0^{rel}$	r_N	$\|\boldsymbol{\varepsilon}_h\|_0^{rel}$	r_N	$\|\boldsymbol{\varepsilon}_h\|_0^{rel}$	r_N	$\|\boldsymbol{\varepsilon}_h\|_0^{rel}$	r_N
1	5	0.26	-1.59	0.26	-1.59	0.13	-2.15	0.61	-0.71
	22	1.48×10^{-2}	-2.02	1.48×10^{-2}	-2.02	5.12×10^{-3}	-2.06	5.32×10^{-2}	-2.0
	100	7.01×10^{-4}	-2.01	7.01×10^{-4}	-2.01	2.41×10^{-4}	-2.0	2.55×10^{-3}	-2.0
2	5	2.3×10^{-2}	-3.13	1.77×10^{-2}	-3.23	9.79×10^{-3}	-3.05	3.1×10^{-2}	-3.3
	22	2.48×10^{-4}	-3.02	1.8×10^{-4}	-3.02	1.14×10^{-4}	-3.0	2.9×10^{-4}	-3.04
	100	2.6×10^{-6}	-3.0	1.9×10^{-6}	-3.0	1.21×10^{-6}	-3.0	3.03×10^{-6}	-3.0
3	5	1.59×10^{-3}	-3.98	1.21×10^{-3}	-4.01	7.41×10^{-4}	-3.98	1.66×10^{-3}	-4.03
	22	4.24×10^{-6}	-4.0	3.22×10^{-6}	-4.0	1.99×10^{-6}	-4.0	4.42×10^{-6}	-4.0
	100	9.88×10^{-9}	-4.0	7.54×10^{-9}	-4.0	4.68×10^{-9}	-4.0	1.03×10^{-8}	-4.0
4	5	9.76×10^{-5}	-4.99	7.55×10^{-5}	-4.98	4.61×10^{-5}	-4.98	9.6×10^{-5}	-4.98
	22	5.89×10^{-8}	-5.0	4.62×10^{-8}	-5.0	2.82×10^{-8}	-5.0	5.88×10^{-8}	-5.0
	100	3.03×10^{-11}	-5.01	2.38×10^{-11}	-5.0	1.46×10^{-11}	-5.0	3.03×10^{-11}	-5.0

TABLE 5. Evolution of the relative error $\|\boldsymbol{\varepsilon}_h\|_0^{rel}$ according to the number of mesh cells N and the polynomial degree k.

		SD_CLo		SD_IG		FR_Radau		FR_G2	
k	N	$\|\boldsymbol{\varepsilon}_h\|_{1,h}^{rel}$	r_N	$\|\boldsymbol{\varepsilon}_h\|_{1,h}^{rel}$	r_N	$\|\boldsymbol{\varepsilon}_h\|_{1,h}^{rel}$	r_N	$\|\boldsymbol{\varepsilon}_h\|_{1,h}^{rel}$	r_N
1	5	0.56	-0.84	0.56	-0.84	0.41	-0.93	0.89	-0.3
	22	0.12	-1.06	0.12	-1.06	9.51×10^{-2}	-1.0	0.2	-1.19
	100	2.43×10^{-2}	-1.01	2.43×10^{-2}	-1.01	2.09×10^{-2}	-1.0	3.81×10^{-2}	-1.05
2	5	0.11	-2.05	0.11	-1.99	7.66×10^{-2}	-1.93	0.15	-2.02
	22	5.64×10^{-3}	-2.01	5.45×10^{-3}	-2.0	4.07×10^{-3}	-2.0	7.45×10^{-3}	-2.0
	100	2.71×10^{-4}	-2.0	2.64×10^{-4}	-2.0	1.97×10^{-4}	-2.0	3.6×10^{-4}	-2.0
3	5	1.48×10^{-2}	-2.98	1.36×10^{-2}	-2.95	9.23×10^{-3}	-2.95	1.73×10^{-2}	-2.95
	22	1.75×10^{-4}	-3.0	1.63×10^{-4}	-3.0	1.11×10^{-4}	-3.0	2.07×10^{-4}	-3.0
	100	1.86×10^{-6}	-3.0	1.74×10^{-6}	-3.0	1.18×10^{-6}	-3.0	2.21×10^{-6}	-3.0
4	5	1.43×10^{-3}	-3.97	1.26×10^{-3}	-3.96	8.09×10^{-4}	-3.96	1.53×10^{-3}	-3.96
	22	3.87×10^{-6}	-4.0	3.43×10^{-6}	-4.0	2.2×10^{-6}	-4.0	4.17×10^{-6}	-4.0
	100	9.07×10^{-9}	-4.0	8.04×10^{-9}	-4.0	5.15×10^{-9}	-4.0	9.78×10^{-9}	-4.0

TABLE 6. Evolution of the relative error $|\boldsymbol{\varepsilon}_h|_{1,h}^{rel}$ according to the number of mesh cells N and the polynomial degree k.

values of L will be considered and the corresponding number of mesh cells are computed as $N = N_{dof/\lambda}\frac{\kappa L}{2\pi(k+1)}$ (which are integers for $\kappa = 2\pi$ and the following choices of $L \in \{0.1, 1, 10\}$).
For a given error norm $|\boldsymbol{\varepsilon}_h|$ and a domain length L (and the corresponding cell number $N > 2$), the estimate of the dependence rate r_L is given thanks to the error norm values for $N \pm 1$ cells (corresponding to $L \pm \delta L$ with $\delta L = \frac{2\pi(k+1)}{\kappa N_{dof/\lambda}}$), respectively denoted $|\boldsymbol{\varepsilon}_h|_{L\pm\delta L}$, as

$$r_L = \frac{\log_{10}(|\boldsymbol{\varepsilon}_h|_{L+\delta L}) - \log_{10}(|\boldsymbol{\varepsilon}_h|_{L-\delta L})}{\log_{10}(L+\delta L) - \log_{10}(L-\delta L)}. \tag{165}$$

Then, Tables 7, 8 and 9 present the values of r_L and the **non-relative** error norms $|\boldsymbol{\varepsilon}_h|_\square$, $\|\boldsymbol{\varepsilon}_h\|_0$ and $|\boldsymbol{\varepsilon}_h|_{1,h}$ respectively, when the domain size is increased, while the number of dof per wavelength is kept constant.

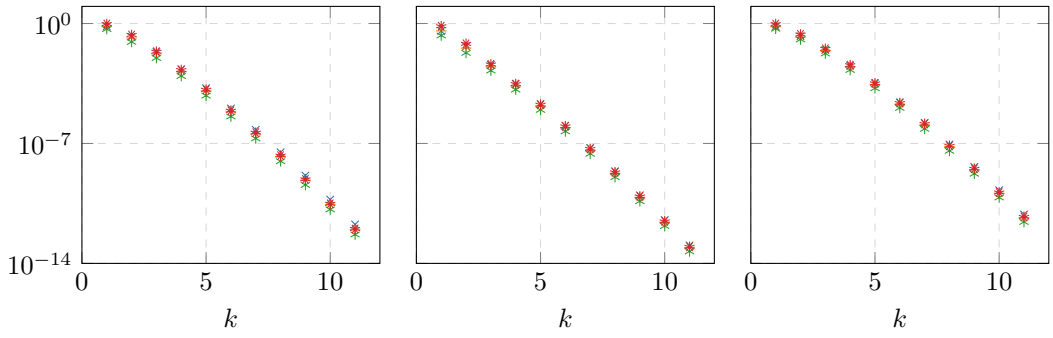

(I) $|\boldsymbol{\varepsilon}_h|_{\square}^{rel}$ (II) $\|\boldsymbol{\varepsilon}_h\|_0^{rel}$ (III) $|\boldsymbol{\varepsilon}_h|_{1,h}^{rel}$

FIGURE 5. Evolution of the relative errors according to the polynomial degree k for the four flux correction families: SD_CLo (×), SD_IG (+), FR_Radau (∗) and FR_G2 (∗).

		SD_CLo		SD_IG		FR_Radau		FR_G2	
k	L	$\|\boldsymbol{\varepsilon}_h\|_{\square}$	r_L	$\|\boldsymbol{\varepsilon}_h\|_{\square}$	r_L	$\|\boldsymbol{\varepsilon}_h\|_{\square}$	r_L	$\|\boldsymbol{\varepsilon}_h\|_{\square}$	r_L
1	0.1	1.12×10^{-3}	0.5	1.12×10^{-3}	0.5	7.43×10^{-4}	0.5	2.23×10^{-3}	0.5
	1.0	3.53×10^{-3}	0.5	3.53×10^{-3}	0.5	2.35×10^{-3}	0.5	7.1×10^{-3}	0.51
	10.0	1.14×10^{-2}	0.52	1.14×10^{-2}	0.52	7.43×10^{-3}	0.5	2.39×10^{-2}	0.56
2	0.1	8.04×10^{-6}	0.5	7.15×10^{-6}	0.5	4.29×10^{-6}	0.5	1.07×10^{-5}	0.5
	1.0	2.54×10^{-5}	0.5	2.26×10^{-5}	0.5	1.36×10^{-5}	0.5	3.39×10^{-5}	0.5
	10.0	8.07×10^{-5}	0.5	7.15×10^{-5}	0.5	4.29×10^{-5}	0.5	1.07×10^{-4}	0.5
3	0.1	5.76×10^{-8}	0.5	4.61×10^{-8}	0.5	2.63×10^{-8}	0.5	6.15×10^{-8}	0.5
	1.0	1.82×10^{-7}	0.5	1.46×10^{-7}	0.5	8.33×10^{-8}	0.5	1.94×10^{-7}	0.5
	10.0	5.77×10^{-7}	0.5	4.61×10^{-7}	0.5	2.63×10^{-7}	0.5	6.15×10^{-7}	0.5
4	0.1	4.12×10^{-10}	0.5	3.01×10^{-10}	0.5	1.67×10^{-10}	0.5	3.77×10^{-10}	0.5
	1.0	1.3×10^{-9}	0.5	9.53×10^{-10}	0.5	5.29×10^{-10}	0.5	1.19×10^{-9}	0.5
	10.0	4.12×10^{-9}	0.5	3.01×10^{-9}	0.5	1.67×10^{-9}	0.5	3.77×10^{-9}	0.5

TABLE 7. Evolution of the non-relative error $|\boldsymbol{\varepsilon}_h|_{\square}$ according to the domain size L, for a constant number of dof per wavelength.

In accordance with the estimates (75) of Theorem 4.6, Remark 4.7 and the flux correction polynomial constants of Table 3, different behaviours can be highlighted:

- Tables 7 and 9 show a $\sqrt{\kappa L}$-dependence of $|\boldsymbol{\varepsilon}_h|_{\square}$ and $|\boldsymbol{\varepsilon}_h|_{1,h}$ on the number of wavelengths in the domain for all the flux correction polynomial families.
- For $\|\boldsymbol{\varepsilon}_h\|_0$, two cases can be detailed.
  First, if $A_k = 0$ (for FR_Radau, and SD_IG and FR_G2 when $k \geqslant 2$), the same $\sqrt{\kappa L}$-dependence is observed. On the contrary, if $A_k > 0$ (for SD_CLo), the $\sqrt{\kappa L}$-dependence only happens when κL tends to 0, while having κL diverging to $+\infty$ implies a $(\kappa L)^{3/2}$-dependence. Moreover, this transition seems to happen for larger values of L when the polynomial degree k increases.

Finally, the estimates (75) highlight the potential interest of flux correction polynomial functions for which $A_k = 0$, as their dependence on the number of wavelengths in the domain is optimised.

		SD_CLo		SD_IG		FR_Radau		FR_G2	
k	L	$\|\boldsymbol{\varepsilon}_h\|_0$	r_L	$\|\boldsymbol{\varepsilon}_h\|_0$	r_L	$\|\boldsymbol{\varepsilon}_h\|_0$	r_L	$\|\boldsymbol{\varepsilon}_h\|_0$	r_L
1	0.1	2.38×10^{-5}	0.53	2.38×10^{-5}	0.53	1.57×10^{-5}	0.5	5.97×10^{-5}	0.57
	1.0	1.44×10^{-4}	1.23	1.44×10^{-4}	1.23	4.96×10^{-5}	0.5	5.25×10^{-4}	1.38
	10.0	3.9×10^{-3}	1.5	3.9×10^{-3}	1.5	1.59×10^{-4}	0.53	1.56×10^{-2}	1.5
2	0.1	1.52×10^{-7}	0.51	1.4×10^{-7}	0.5	8.88×10^{-8}	0.5	2.22×10^{-7}	0.5
	1.0	6.02×10^{-7}	0.86	4.41×10^{-7}	0.5	2.81×10^{-7}	0.5	7.02×10^{-7}	0.5
	10.0	1.16×10^{-5}	1.48	1.41×10^{-6}	0.52	8.88×10^{-7}	0.5	2.26×10^{-6}	0.54
3	0.1	9.94×10^{-10}	0.5	8.75×10^{-10}	0.5	5.42×10^{-10}	0.5	1.2×10^{-9}	0.5
	1.0	3.62×10^{-9}	0.75	2.77×10^{-9}	0.5	1.71×10^{-9}	0.5	3.79×10^{-9}	0.5
	10.0	5.78×10^{-8}	1.47	8.75×10^{-9}	0.5	5.42×10^{-9}	0.5	1.2×10^{-8}	0.5
4	0.1	6.59×10^{-12}	0.5	5.63×10^{-12}	0.5	3.43×10^{-12}	0.5	7.15×10^{-12}	0.5
	1.0	2.26×10^{-11}	0.65	1.78×10^{-11}	0.5	1.09×10^{-11}	0.5	2.26×10^{-11}	0.5
	10.0	2.82×10^{-10}	1.5	5.63×10^{-11}	0.5	3.44×10^{-11}	0.51	7.15×10^{-11}	0.5

TABLE 8. Evolution of the non-relative error $\|\boldsymbol{\varepsilon}_h\|_0$ according to the domain size L, for a constant number of dof per wavelength.

		SD_CLo		SD_IG		FR_Radau		FR_G2	
k	L	$\|\boldsymbol{\varepsilon}_h\|_{1,h}$	r_L	$\|\boldsymbol{\varepsilon}_h\|_{1,h}$	r_L	$\|\boldsymbol{\varepsilon}_h\|_{1,h}$	r_L	$\|\boldsymbol{\varepsilon}_h\|_{1,h}$	r_L
1	0.1	2.95×10^{-2}	0.5	2.95×10^{-2}	0.5	2.57×10^{-2}	0.5	4.47×10^{-2}	0.5
	1.0	9.37×10^{-2}	0.5	9.37×10^{-2}	0.5	8.14×10^{-2}	0.5	0.14	0.52
	10.0	0.31	0.55	0.31	0.55	0.26	0.5	0.52	0.65
2	0.1	2.49×10^{-4}	0.5	2.43×10^{-4}	0.5	1.82×10^{-4}	0.5	3.32×10^{-4}	0.5
	1.0	7.88×10^{-4}	0.5	7.7×10^{-4}	0.5	5.75×10^{-4}	0.5	1.05×10^{-3}	0.5
	10.0	2.52×10^{-3}	0.51	2.43×10^{-3}	0.5	1.82×10^{-3}	0.5	3.32×10^{-3}	0.5
3	0.1	2.03×10^{-6}	0.5	1.9×10^{-6}	0.5	1.29×10^{-6}	0.5	2.41×10^{-6}	0.5
	1.0	6.42×10^{-6}	0.5	6.0×10^{-6}	0.5	4.08×10^{-6}	0.5	7.64×10^{-6}	0.5
	10.0	2.04×10^{-5}	0.51	1.9×10^{-5}	0.5	1.29×10^{-5}	0.5	2.41×10^{-5}	0.5
4	0.1	1.61×10^{-8}	0.5	1.43×10^{-8}	0.5	9.17×10^{-9}	0.5	1.74×10^{-8}	0.5
	1.0	5.1×10^{-8}	0.5	4.52×10^{-8}	0.5	2.9×10^{-8}	0.5	5.5×10^{-8}	0.5
	10.0	1.62×10^{-7}	0.5	1.43×10^{-7}	0.5	9.17×10^{-8}	0.5	1.74×10^{-7}	0.5

TABLE 9. Evolution of the non-relative error $|\boldsymbol{\varepsilon}_h|_{1,h}$ according to the domain size L, for a constant number of dof per wavelength.

6. Time-harmonic 3D Maxwell problem: error analysis through numerical experiments

Finally, we come back to the Maxwell Problem 1.4. Contrary to the 1D wave problem, we did not derive a priori error estimates for this case. Yet, we present numerical results for the implementation of the FR formulation associated to the numerical traces introduced in Remark 3.3 of Subsection 3.2.
We consider a domain $\Omega = [0, L]^3$, with a uniform mesh of N cells of size $h = \frac{L}{N}$ in each direction. In all the following experiments, we consider the parameters summarised in Table 10 with uniform polynomial degree k and flux correction polynomial functions in all the cells and every direction (even if direction-wise choices could have been made). Finally, we take back the four flux correction polynomial families introduced in Section 5 to compare their influence in this 3D configuration.

Moreover, we consider impedance boundary conditions associated to an exact solution $\mathbb{E}_{exa} = (\mathbf{e}_{exa}, \mathbf{h}_{exa})$ of

κ	L	ε_r	μ_r	$Z_{\partial\Omega}$	$\mathbf{k}_{pw}$	$\mathbf{e}_{pw}$	$\mathbf{h}_{pw}$	$\mathbf{P}_d$	$\mathbf{X}_d$
2π	1	1	1	1	$2^{1/2}\pi(1,-1,0)$	$(0,0,1)$	$-2^{-1/2}(1,1,0)$	$2^{-1/2}(1,-1,0.)$	$-0.5(1,1,1)$

TABLE 10. Common characteristics and parameters of the different simulation configurations.

the Maxwell problem, which leads to:

$$\mathbf{g} \;=\; \gamma_t \mathbf{e}_{exa} \;+\; Z_{\partial\Omega}\, \mathbf{n}_{\partial\Omega} \times \gamma_t \mathbf{h}_{exa} \quad \text{ on } \partial\Omega, \tag{166}$$

and the numerical approximation $\mathbb{E}_{\mathbf{h}}$ is thus compared to $\mathbb{E}_{exa}$ thanks to the error $\boldsymbol{\varepsilon}_{\mathbf{h}} = \mathbb{E}_{exa} - \mathbb{E}_{\mathbf{h}}$.
Finally, we consider two different exact solutions, whose parameters are summarised in Table 10:

- A Plane Wave defined by

$$\forall\, \mathbf{x} \in \Omega, \quad \mathbf{e}_{exa}(\mathbf{x}) = \mathbf{e}_{pw} e^{i\mathbf{k}_{pw}\cdot\mathbf{x}} \quad \text{ and } \quad \mathbf{h}_{exa}(\mathbf{x}) = \mathbf{h}_{pw} e^{i\mathbf{k}_{pw}\cdot\mathbf{x}}, \tag{167}$$

  where $\mathbf{k}_{pw} \times \mathbf{e}_{pw} = -\kappa\mu_r \mathbf{h}_{pw}$ and $\mathbf{k}_{pw} \times \mathbf{h}_{pw} = \kappa\epsilon_r \mathbf{e}_{pw}$.
- An electric dipole of dipole moment $\mathbf{P}_d$ and position $\mathbf{X}_d$, defined in the framework of the dipole approximation [25] by

$$\forall\, \mathbf{x} \in \Omega, \; \left\{ \begin{array}{rcl} \mathbf{e}_{exa}(\mathbf{x}) & = & \dfrac{e^{-i\kappa r}}{4\pi r}\left[\left(-\dfrac{1}{r^2} - \dfrac{i\kappa}{r} + \kappa^2\right)\left(\widetilde{\mathbf{x}} \times (\mathbf{P} \times \widetilde{\mathbf{x}})\right) + 2\left(\dfrac{1}{r^2} + \dfrac{i\kappa}{r}\right)(\mathbf{P}\cdot\widetilde{\mathbf{x}})\,\widetilde{\mathbf{x}}\right], \\ \mathbf{h}_{exa}(\mathbf{x}) & = & \dfrac{e^{-i\kappa r}}{4\pi r}\left(-\dfrac{i\kappa}{r} + \kappa^2\right)(\widetilde{\mathbf{x}} \times \mathbf{P}), \end{array} \right. \tag{168}$$

  where we denote $r = \|\mathbf{x} - \mathbf{X}_d\|$ and $\widetilde{\mathbf{x}} = \dfrac{\mathbf{x} - \mathbf{X}_d}{r}$.

Thus, we focus on the h-convergence of the formulation. We fix all the parameters and we make the number of cells in each direction, N, vary: the goal is to highlight the effect of mesh refinement on the error $\boldsymbol{\varepsilon}_{\mathbf{h}}$.
Moreover, the convergence rate is evaluated in a similar way as in Subsection 5.3 (see (164)).
Tables 11 and 12 present the relative L^2-norm error $\|\boldsymbol{\varepsilon}_{\mathbf{h}}\|_0^{rel}$, for the two exact solutions, when the number of cells per direction increases. For all the flux correction polynomial functions and polynomial degrees k, it shows an asymptotic quasi-optimal behaviour, as it was previously proved in the 1D case, and highlights properties of a high-order method. Moreover, the flux correction polynomial family hierarchy seems to be the same as in the 1D wave equations case: FR_Radau clearly presents the best abilities in these contexts.

Remark 6.1. One will note that the finest mesh refinements are not presented for the highest polynomial degrees in Tables 11 and 12: this is due to the fact these cases imply a prohibitive memory cost (due to the direct resolution of the linear system) which prevented us from computing the associated results.

CONCLUSION

We introduced a Flux Reconstruction method in the framework of generic time-harmonic linear hyperbolic problems, for Cartesian meshes of hyperrectangular domains. It relies on the piecewise polynomial approximation of the solution and fluxes, thanks to interface corrections to impose boundary conditions and flux continuity. Such perturbations are realised thanks to user-dependent flux correction polynomial functions, whose choice allows to recover some classical methods (as nodal Discontinuous Galerkin or Spectral Difference). A general flux numerical trace definition through flux operator decomposition is also detailed, and the associated FR methods have been specified for the homogeneous 1D time-harmonic wave equations and the 3D Maxwell problem.
Then, we focused on the 1D wave equations with ingoing boundary conditions, for which well-posedness conditions of the associated FR method have been derived. This also allowed to determine quasi-optimal a priori

		SD_CLo		SD_IG		FR_Radau		FR_G2	
k	N	$\|\boldsymbol{\varepsilon}_\mathbf{h}\|_0^{rel}$	r_N	$\|\boldsymbol{\varepsilon}_\mathbf{h}\|_0^{rel}$	r_N	$\|\boldsymbol{\varepsilon}_\mathbf{h}\|_0^{rel}$	r_N	$\|\boldsymbol{\varepsilon}_\mathbf{h}\|_0^{rel}$	r_N
1	3	0.29	-1.42	0.29	-1.42	0.19	-1.82	0.54	-0.69
	5	0.12	-1.83	0.12	-1.83	6.77×10^{-2}	-2.03	0.31	-1.37
	9	3.91×10^{-2}	-1.97	3.91×10^{-2}	-1.97	2.04×10^{-2}	-2.03	0.12	-1.84
	12	2.21×10^{-2}	-1.98	2.21×10^{-2}	-1.98	1.14×10^{-2}	-2.02	6.8×10^{-2}	-1.92
	19	8.87×10^{-3}	-1.99	8.87×10^{-3}	-1.99	4.54×10^{-3}	-2.01	2.78×10^{-2}	-1.97
	31	3.34×10^{-3}	-2.0	3.34×10^{-3}	-2.0	1.7×10^{-3}	-2.0	1.06×10^{-2}	-1.98
2	3	3.82×10^{-2}	-2.88	3.33×10^{-2}	-2.93	2.12×10^{-2}	-2.97	5.19×10^{-2}	-2.84
	5	8.47×10^{-3}	-2.97	7.24×10^{-3}	-3.0	4.62×10^{-3}	-2.99	1.14×10^{-2}	-2.98
	9	1.47×10^{-3}	-2.99	1.24×10^{-3}	-3.0	7.97×10^{-4}	-2.99	1.97×10^{-3}	-2.99
	12	6.21×10^{-4}	-2.99	5.25×10^{-4}	-3.0	3.37×10^{-4}	-3.0	8.34×10^{-4}	-2.99
	19	1.57×10^{-4}	-3.0	1.33×10^{-4}	-3.0	8.5×10^{-5}	-3.0	2.11×10^{-4}	-2.99
3	3	3.52×10^{-3}	-3.88	3.02×10^{-3}	-3.93	1.92×10^{-3}	-3.95	4.06×10^{-3}	-3.9
	5	4.73×10^{-4}	-3.95	4.0×10^{-4}	-3.97	2.53×10^{-4}	-3.98	5.44×10^{-4}	-3.95
	9	4.58×10^{-5}	-3.98	3.86×10^{-5}	-3.99	2.42×10^{-5}	-3.99	5.28×10^{-5}	-3.98
	12	1.45×10^{-5}	-3.99	1.23×10^{-5}	-3.99	7.68×10^{-6}	-4.0	1.68×10^{-5}	-3.99
4	3	2.7×10^{-4}	-4.9	2.25×10^{-4}	-4.92	1.41×10^{-4}	-4.95	2.83×10^{-4}	-4.9
	5	2.16×10^{-5}	-4.96	1.79×10^{-5}	-4.97	1.11×10^{-5}	-4.98	2.27×10^{-5}	-4.96
	9	1.16×10^{-6}	-4.99	9.6×10^{-7}	-4.99	5.94×10^{-7}	-4.99	1.22×10^{-6}	-4.98

TABLE 11. Evolution of the relative error $\|\boldsymbol{\varepsilon}_\mathbf{h}\|_0^{rel}$ according to the number of mesh cells N for the Plane Wave.

		SD_CLo		SD_IG		FR_Radau		FR_G2	
k	N	$\|\boldsymbol{\varepsilon}_\mathbf{h}\|_0^{rel}$	r_N	$\|\boldsymbol{\varepsilon}_\mathbf{h}\|_0^{rel}$	r_N	$\|\boldsymbol{\varepsilon}_\mathbf{h}\|_0^{rel}$	r_N	$\|\boldsymbol{\varepsilon}_\mathbf{h}\|_0^{rel}$	r_N
1	3	0.26	-1.42	0.26	-1.42	0.17	-1.83	0.5	-0.67
	5	0.11	-1.82	0.11	-1.82	6.16×10^{-2}	-2.04	0.29	-1.37
	9	3.61×10^{-2}	-1.97	3.61×10^{-2}	-1.97	1.85×10^{-2}	-2.03	0.11	-1.85
	12	2.04×10^{-2}	-1.98	2.04×10^{-2}	-1.98	1.04×10^{-2}	-2.02	6.37×10^{-2}	-1.92
	19	8.19×10^{-3}	-1.99	8.19×10^{-3}	-1.99	4.11×10^{-3}	-2.01	2.6×10^{-2}	-1.97
	31	3.08×10^{-3}	-2.0	3.08×10^{-3}	-2.0	1.54×10^{-3}	-2.0	9.87×10^{-3}	-1.99
2	3	3.67×10^{-2}	-2.86	3.15×10^{-2}	-2.91	2.01×10^{-2}	-2.96	4.9×10^{-2}	-2.82
	5	8.15×10^{-3}	-2.97	6.86×10^{-3}	-2.99	4.39×10^{-3}	-2.98	1.08×10^{-2}	-2.98
	9	1.41×10^{-3}	-2.99	1.18×10^{-3}	-2.99	7.58×10^{-4}	-2.99	1.87×10^{-3}	-2.99
	12	5.96×10^{-4}	-3.0	4.99×10^{-4}	-2.99	3.2×10^{-4}	-3.0	7.89×10^{-4}	-2.99
	19	1.5×10^{-4}	-3.0	1.26×10^{-4}	-2.99	8.08×10^{-5}	-3.0	2.0×10^{-4}	-2.99
3	3	3.75×10^{-3}	-3.85	3.2×10^{-3}	-3.9	2.05×10^{-3}	-3.93	4.29×10^{-3}	-3.87
	5	5.08×10^{-4}	-3.94	4.27×10^{-4}	-3.96	2.7×10^{-4}	-3.98	5.79×10^{-4}	-3.94
	9	4.94×10^{-5}	-3.98	4.13×10^{-5}	-3.98	2.6×10^{-5}	-3.99	5.63×10^{-5}	-3.97
	12	1.57×10^{-5}	-3.99	1.31×10^{-5}	-3.99	8.23×10^{-6}	-3.99	1.79×10^{-5}	-3.98
4	3	3.42×10^{-4}	-4.86	2.85×10^{-4}	-4.89	1.79×10^{-4}	-4.93	3.56×10^{-4}	-4.87
	5	2.76×10^{-5}	-4.95	2.28×10^{-5}	-4.96	1.42×10^{-5}	-4.97	2.88×10^{-5}	-4.95
	9	1.48×10^{-6}	-4.98	1.23×10^{-6}	-4.98	7.57×10^{-7}	-4.99	1.55×10^{-6}	-4.98

TABLE 12. Evolution of the relative error $\|\boldsymbol{\varepsilon}_\mathbf{h}\|_0^{rel}$ according to the number of mesh cells N for the dipole.

error estimates in the asymptotic limit for various error norms, with explicit expressions of the constants in terms of the polynomial degree, flux correction polynomials, wavenumber, domain length and mesh properties. Numerical experiments were realised for some classical flux correction polynomial families, and confirmed the expected behaviours of the estimates in terms of the mesh refinement, polynomial degree and dependence on the number of wavelengths in the domain.
Finally, the FR method has been implemented for the 3D time-harmonic Maxwell problem. Even if a priori estimates were not derived in this case, numerical experiments highlighted quasi-optimal orders for two different actual solutions and allow to expect this method to show interesting properties for wave equations.

The presented approach relied on the possibility to uncouple the 1D wave equations thanks to the one-way variables, and further developments may be needed to extend this work to general boundary conditions or heterogeneous materials: in case this strong framework would not be applicable anymore, one could contemplate classic methodology for the associated weak formulation. The same remark holds in the 3D framework of the Maxwell problem, for which it seems difficult to introduce uncoupling variables (which would rely on the simultaneously diagonalisable character of the flux operators).
Furthermore, optimisations may be applied to such a method: one can think about Domain Decomposition Methods [9, 12, 28] or static condensation [34] as for example Hybrid Discontinuous Galerkin (HDG) [6, 32, 33] or Hybrid High Order (HHO) [31, 36], allowing to reduce the amount of degrees of freedom.
This work allowed to explicit the influence of the error norms with respect to the flux correction polynomial functions and discretisation parameters. Numerically, the Radau polynomials (corresponding to a nodal DG method) led to the best results in both these time-harmonic frameworks, in comparison with the SD and G2 corrections. Then, the explicit character of the 1D estimates allows to get a glimpse of the possibility to optimise their constants according to the flux correction polynomial, which will be investigated in further work in order to define an 'optimised' FR scheme.

References

[1] M. Ainsworth, Peter Monk, and W. Muniz. Dispersive and Dissipative Properties of Discontinuous Galerkin Finite Element Methods for the Second-Order Wave Equation. *J. Sci. Comput.*, 27:5–40, June 2006.
[2] Y. Allaneau and A. Jameson. Connections between the filtered discontinuous Galerkin method and the flux reconstruction approach to high order discretizations. *Computer Methods in Applied Mechanics and Engineering*, 200(49):3628–3636, December 2011.
[3] Alain Bossavit. *Computational electromagnetism: variational formulations, complementarity, edge elements*. Academic Press, 1998.
[4] Annalisa Buffa, Martin Costabel, and Christoph Schwab. Boundary element methods for Maxwell's equations on non-smooth domains. *Numerische Mathematik*, 92:679–710, October 2002.
[5] Patrice Castonguay, Peter Vincent, and Antony Jameson. Application of High-Order Energy Stable Flux Reconstruction Schemes to the Euler Equations. In *49th AIAA Aerospace Sciences Meeting including the New Horizons Forum and Aerospace Exposition*, Orlando, Florida, January 2011. American Institute of Aeronautics and Astronautics.
[6] Bernardo Cockburn, Jayadeep Gopalakrishnan, and Raytcho Lazarov. Unified Hybridization of Discontinuous Galerkin, Mixed, and Continuous Galerkin Methods for Second Order Elliptic Problems. *SIAM Journal on Numerical Analysis*, 47(2):1319–1365, January 2009. Publisher: Society for Industrial and Applied Mathematics.
[7] Gary Cohen and Sébastien Pernet. *Finite Element and Discontinuous Galerkin Methods for Transient Wave Equations*. Scientific Computation. Springer Netherlands, Dordrecht, 2017.
[8] Gary C. Cohen. *Higher-Order Numerical Methods for Transient Wave Equations*. Scientific Computation. Springer, Berlin, Heidelberg, 2002.
[9] Francis Collino, Patrick Joly, and Matthieu Lecouvez. Exponentially convergent non overlapping domain decomposition methods for the Helmholtz equation. *ESAIM: Mathematical Modelling and Numerical Analysis*, 54(3):775–810, May 2020.
[10] Daniele Antonio Di Pietro and Alexandre Ern. *Mathematical Aspects of Discontinuous Galerkin Methods*, volume 69 of *Mathématiques et Applications*. Springer, Berlin, Heidelberg, 2012.
[11] Alexandre Ern, Jean-Luc Guermond, and Gilbert Caplain. An Intrinsic Criterion for the Bijectivity of Hilbert Operators Related to Friedrich' Systems. *Communications in Partial Differential Equations*, 32:317–341, February 2007.

[12] O. G. Ernst and M. J. Gander. Why it is Difficult to Solve Helmholtz Problems with Classical Iterative Methods. In Ivan G. Graham, Thomas Y. Hou, Omar Lakkis, and Robert Scheichl, editors, *Numerical Analysis of Multiscale Problems*, Lecture Notes in Computational Science and Engineering, pages 325–363. Springer, Berlin, Heidelberg, 2012.

[13] K. O. Friedrichs. Symmetric positive linear differential equations. *Communications on Pure and Applied Mathematics*, 11(3):333–418, 1958.

[14] Arijit Hazra, Praveen Chandrashekar, and Dinshaw S. Balsara. Globally constraint-preserving FR/DG scheme for Maxwell's equations at all orders. *Journal of Computational Physics*, 394:298–328, October 2019.

[15] J. S. Hesthaven and T. Warburton. High–order nodal discontinuous Galerkin methods for the Maxwell eigenvalue problem. *Philosophical Transactions of the Royal Society of London. Series A: Mathematical, Physical and Engineering Sciences*, 362(1816):493–524, March 2004.

[16] R. Hiptmair. Finite elements in computational electromagnetism. *Acta Numerica*, 11:237–339, January 2002. Publisher: Cambridge University Press.

[17] Paul Houston, Ilaria Perugia, Anna Schneebeli, and Dominik Schötzau. Interior penalty method for the indefinite time-harmonic Maxwell equations. *Numerische Mathematik*, 100(3):485–518, May 2005.

[18] Paul Houston, Ilaria Perugia, Anna Schneebeli, and Dominik Schötzau. Mixed discontinuous Galerkin approximation of the Maxwell operator: The indefinite case. *ESAIM: Mathematical Modelling and Numerical Analysis*, 39(4):727–753, July 2005. Number: 4 Publisher: EDP Sciences.

[19] Paul Houston, Bill Senior, and Endre Süli. hp-Discontinuous Galerkin finite element methods for hyperbolic problems: error analysis and adaptivity. *International Journal for Numerical Methods in Fluids*, 40(1-2):153–169, 2002.

[20] H.T. Huynh. A Flux Reconstruction Approach to High-Order Schemes Including Discontinuous Galerkin Methods. *AIAA Paper AIAA 20074079*, pages 1–42, January 2007.

[21] H.T. Huynh, Z. Wang, and P.E. Vincent. High-Order Methods for Computational Fluid Dynamics: A Brief Review of Compact Differential Formulation on Unstructured Grids. *Computers & Fluids*, 98, June 2013.

[22] Antony Jameson. A Proof of the Stability of the Spectral Difference Method for All Orders of Accuracy. *Journal of Scientific Computing*, 45(1):348–358, October 2010.

[23] Jian-Ming Jin. *The finite element method in electromagnetics*. John Wiley & Sons, 2015.

[24] David A. Kopriva and John H. Kolias. A Conservative Staggered-Grid Chebyshev Multidomain Method for Compressible Flows. *Journal of Computational Physics*, 125(1):244–261, April 1996.

[25] Justine Labat. *Multi-scale modeling of the electromagnetic wave scattering by small obstacles*. phdthesis, Université de Pau et des Pays de l'Adour, November 2019.

[26] Yen Liu, Marcel Vinokur, and Z.J. Wang. Spectral difference method for unstructured grids I: Basic formulation. *Journal of Computational Physics*, 216(2):780–801, August 2006.

[27] Thomas Marchal, Hugues Deniau, and Guillaume Puigt. Entropy-Stable Spectral Difference and Flux Reconstruction Methods for Discontinuous Flows, September 2023. Available at SSRN: http://dx.doi.org/10.2139/ssrn.4569572.

[28] Axel Modave, Xavier Antoine, and Christophe Geuzaine. An efficient domain decomposition method with cross-point treatment for Helmholtz problems. In *CSMA 2019 - 14e Colloque National en Calcul des Structures*, Giens (Var), France, May 2019.

[29] Alireza H. Mohammadian, Vijaya Shankar, and William F. Hall. Computation of electromagnetic scattering and radiation using a time-domain finite-volume discretization procedure. *Computer Physics Communications*, 68(1-3):175–196, November 1991.

[30] Peter Monk. *Finite element methods for Maxwell's equations*. Oxford University Press, 2003.

[31] Emmanuel Montseny, Sébastien Pernet, Xavier Ferrières, and Gary Cohen. Dissipative terms and local time-stepping improvements in a spatial high order discontinuous galerkin scheme for the time-domain maxwell's equations. *Journal of computational physics*, 227(14):6795–6820, 2008.

[32] D Moro, NC Nguyen, and J Peraire. A hybridized discontinuous petrov–galerkin scheme for scalar conservation laws. *International journal for numerical methods in engineering*, 91(9):950–970, 2012.

[33] N. C. Nguyen, J. Peraire, and B. Cockburn. Hybridizable discontinuous Galerkin methods for the time-harmonic Maxwell's equations. *Journal of Computational Physics*, 230(19):7151–7175, August 2011.

[34] Carlos A Pereira and Brian C Vermeire. Hybridized formulations of flux reconstruction schemes for advection-diffusion problems. *arXiv preprint arXiv:2310.15870*, 2023.

[35] Ilaria Perugia and Dominik Schötzau. The hp-local discontinuous Galerkin method for low-frequency time-harmonic Maxwell equations. *Mathematics of Computation*, 72(243):1179–1214, July 2003.

[36] Daniele Di Antonio Pietro and Jerome Droniou. *The Hybrid High-Order Method for Polytopal Meshes: Design, Analysis, and Applications*. Springer, 2020.

[37] Valentin Ritzenthaler, Pierre Cantin, Xavier Ferrières, Sébastien Pernet, and Guillaume Puigt. Spectral Difference method On Structured-Grids for Maxwell's Equations in Time Domain. In *WAVES 2022*, Palaiseau, France, July 2022.

[38] Stefan A. Sauter and Christoph Schwab. *Boundary Element Methods*, volume 39 of *Springer Series in Computational Mathematics*. Springer, Berlin, Heidelberg, 2011.

[39] Margot Sirdey. *Méthode itérative de Trefftz pour la simulation d'ondes électromagnétiques en trois dimensions*. Theses, Université de Pau et des Pays de l'Adour, December 2022.

[40] Allen Taflove and S. Hagness. *Computational electrodynamics: the finite-difference time-domain method. 2nd ed*, volume 67–106. Artech House Publishers, June 2000.

[41] Kris Van den Abeele, Chris Lacor, and Z. J. Wang. On the Stability and Accuracy of the Spectral Difference Method. *Journal of Scientific Computing*, 37(2):162–188, November 2008.

[42] P. E. Vincent, P. Castonguay, and A. Jameson. Insights from von Neumann analysis of high-order flux reconstruction schemes. *Journal of Computational Physics*, 230(22):8134–8154, September 2011.

[43] P. E. Vincent, P. Castonguay, and A. Jameson. A New Class of High-Order Energy Stable Flux Reconstruction Schemes. *Journal of Scientific Computing*, 47(1):50–72, April 2011.

[44] Z. J. Wang and Haiyang Gao. A unifying lifting collocation penalty formulation including the discontinuous Galerkin, spectral volume/difference methods for conservation laws on mixed grids. *Journal of Computational Physics*, 228(21):8161–8186, November 2009.

[45] Z. J. Wang and H. T. Huynh. A review of flux reconstruction or correction procedure via reconstruction method for the Navier-Stokes equations. *Mechanical Engineering Reviews*, 3(1):15–00475–15–00475, 2016.

[46] Kane Yee. Numerical solution of initial boundary value problems involving maxwell's equations in isotropic media. *IEEE Transactions on Antennas and Propagation*, 14(3):302–307, May 1966. Conference Name: IEEE Transactions on Antennas and Propagation.